4.3.2 Shock formation timing

In Chapter II, I argued that a shock would become possible when the ion-ion mean free path, λ_{MFP}, became less than the scale length of the system, L. This visible light data of both the colliding jet experiments and the accretion shock experiments provide an opportunity to test that argument. Figure 4.9 shows region plots in ρ–u space. The blue area is the region where $\lambda_{\mathrm{MFP}} > L$ and a shock should not be able to form; the blank space is the area where $\lambda_{\mathrm{MFP}} < L$ and a shock should be possible. The plots differ due to temperature because of ionization; all other things being equal, higher ionization lowers the MFP and a shock would be possible at lower density/higher velocity. The black points in Figure 4.9 show the trajectory of an isothermal rarefaction at the given temperature across ρ–u space. As seen in Figure 4.9, the 6-eV rarefaction crosses into shock territory at 18 ns, while the 1.6-eV rarefaction crosses at 40 ns. This is in good agreement with the visible image data presented in 4.8.

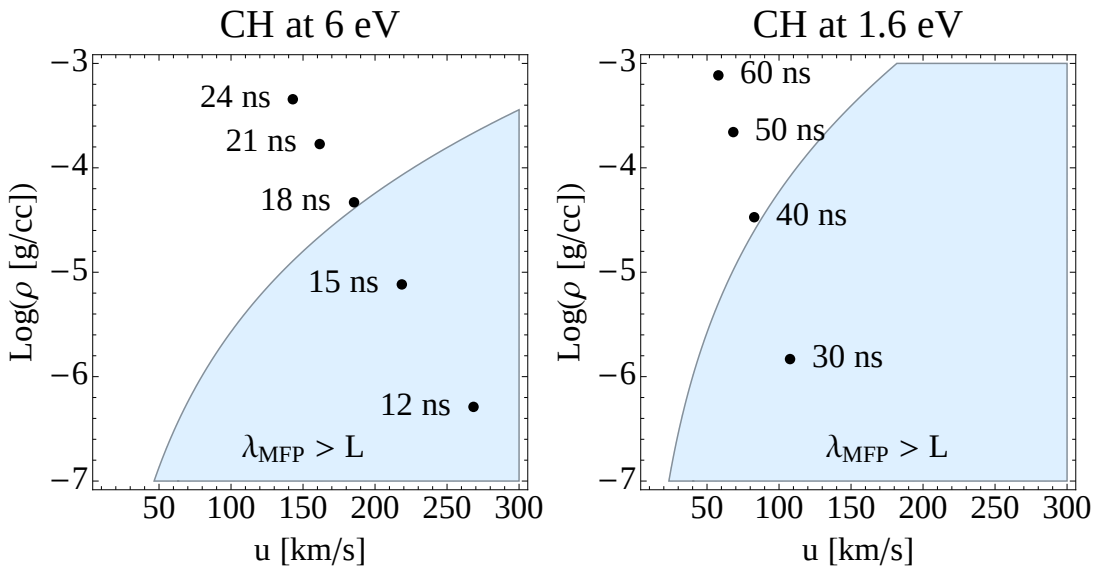

Figure 4.9: Isothermal rarefactions move from the $\lambda_{\mathrm{MFP}} > L$ region into the $\lambda_{\mathrm{MFP}} < L$ region with time.

4.3.3 Shock growth

As seen the no-field series of shots, the scaled accretion shock begins growing around $\sim 40\,\mathrm{ns}$ and reaches a height of $1.2\,\mathrm{mm}$ above above the impact surface by $63\,\mathrm{ns}$. This suggests that the shock surface is rising by $\sim 50\,\mathrm{km\,s^{-1}}$. Is this reasonable?

Figure 4.10 illustrates two frames of reference for the experiment. In the laboratory frame, the incoming velocity is u_{jet}, the velocity downstream of the shock is zero, and the shock front is moving towards the incoming flow ("upward," if the incoming flow is falling "down") at u_s. This is necessary to fulfill the boundary condition at the surface of the block. In the shock frame, the incoming velocity is u_1, the shock is stationary, and the outgoing velocity is u_2. (In the shock frame, the block would have velocity u_2 as well.)

According to the strong shock limit (*Drake*, 2006),

$$u_2 = u_1 \frac{\gamma - 1}{\gamma + 1}, \tag{4.1}$$

where γ is the adiabatic index.

Therefore the laboratory frame is moving up at $u1(\gamma - 1)/(\gamma + 1)$ relative to the shock frame. The downward velocity of the incoming jet is

$$u_{jet} = u_1 - u_1 \frac{\gamma - 1}{\gamma + 1} = u_1 \frac{2}{\gamma + 1}. \tag{4.2}$$

The upward velocity of the shock is

$$u_s = u_1 \frac{\gamma - 1}{\gamma + 1} = u_{jet} \frac{\gamma - 1}{2}. \tag{4.3}$$

So the rough $\sim 50\,\mathrm{km\,s^{-1}}$ upwards growth estimated above would be expected if $u_{jet} = 150\,\mathrm{km\,s^{-1}}$ and $\gamma = 5/3$, but that jet velocity is well above the velocity of an isothermal 1.6-eV jet over this time range, $u_{jet} = 60$–$80\,\mathrm{km\,s^{-1}}$.

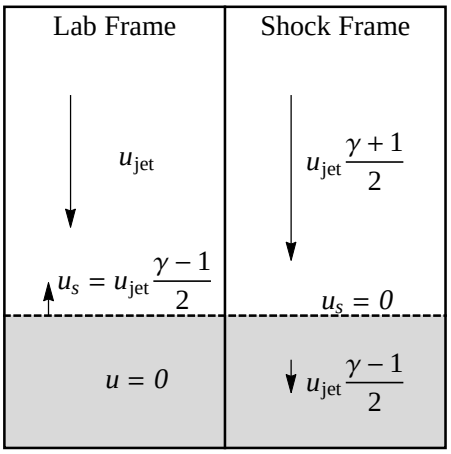

Figure 4.10: The lab vs. the shock frame. In the lab frame, the block is stationary, while in the shock frame, the shock is.

A more precise calculation of shock column height does not solve the discrepancy between predicted and observed growth. I calculated the growth of the shock column by taking

$$h_n = h_{n-1} + dt u_s(h_{n-1}, t_{n-1}), \tag{4.4}$$

where h_n is the height at time t_n, dt is the time step, and u_s is a function of height and time,

$$u_s(h,t) = \frac{\gamma-1}{2} u_{iso}(0.3\,\text{mm} - h, t), \tag{4.5}$$

where u_{iso} is the velocity of an isothermal rarefaction.

Using this method I found that the shock column ought to grow to 0.5 mm between the shock forming at 39 ns and the final image being taken at 63 ns. Consistent with the rough growth estimated above, the measured height of 1.2 ± 0.1 mm is roughly twice the predicted height. Why? It is possible that the intensity jump around $x = 1.8 \pm 0.1$ mm is not a shock at all; the visible light images seen in Figure 4.7 show variation in emitted intensity, which does not necessarily translate to density. It it also possible that flows are coming off the walls of the target and squeezing the shock column and to make it taller than it would otherwise be; this is discussed in Chapter V

because proton radiography data supports the presence of flows coming off the walls. A third possibility is that x-ray pre-heating of the solid impact surface produced yet another plasma rarefaction that expands upward. This rarefaction would collide with the incoming "accreting material" and contribute to the observed height of the "accretion shock column."

4.4 Scaling Revisited

This section revisits the scaling arguments presented in Chapter II. In Chapter II, I argued that the experiment would be well-scaled if five dimensionless number criteria were met; these related to Mach number, ion-ion mean free path, magnetic diffusion length, ram plasma β, and Reynolds number. I constructed region plots showing the area where all five were simultaneously met for either a 10-eV CH plasma or a 30-eV CH plasma in an imposed magnetic field of 10 T.

But the experiment that was actually performed did not involve a 10-T field or a 10-eV or 30-eV plasma. The maximum field that we were able to impose was 7 T, and, as discussed in Section 4.3, for the visible light time series data, the incoming jets had $T_e = 1.6\,\mathrm{eV}$ (one drive beams). Figures 4.11 shows criteria region plots for the 10-T, 10-eV experiment from Chapter II and Figure 4.12 shows the 7-T, 1.6-eV experiment that was performed, respectively.

Lowering the imposed field and the temperature of the flow has several effects on the criteria region plots. First, the yellow region (Mach number too low) is blank in the 1.6-eV plot. At $T_e = 1.6\,\mathrm{eV}$ the entire plot region is acceptable; lower temperature yields a higher Mach number for a given velocity. Second, the blue region (mean free path too large) is larger in the 1.6-eV plot than the original 6-eV one. As temperature falls, ionization goes down and MFP will increase, so the area where MFP is too large with expand. Third, the allowed region where β_{ram} is neither too low nor too high shifts toward lower left corner (low density, low velocity) because the magnetic field

strength has dropped. Together, these changes dramatically shrink the allowed region. (The magnetic diffusion length and the Reynolds number plots seem little affected.)

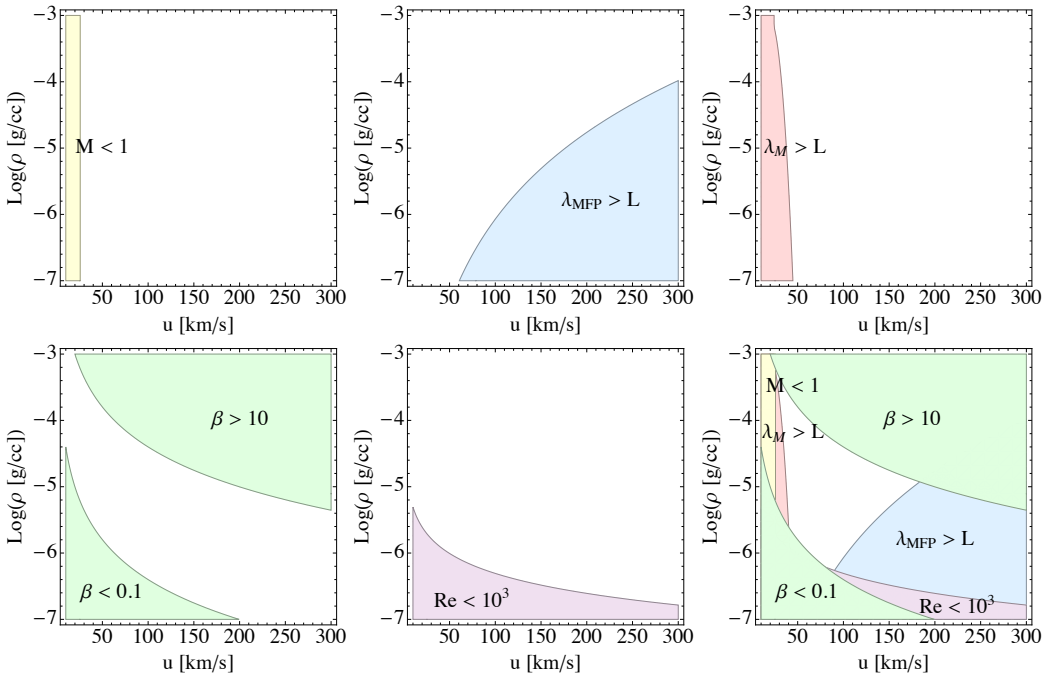

Figure 4.11: Experimental criteria region plots for $T_e = 10\,\mathrm{eV}$ and $B = 10\,\mathrm{T}$.

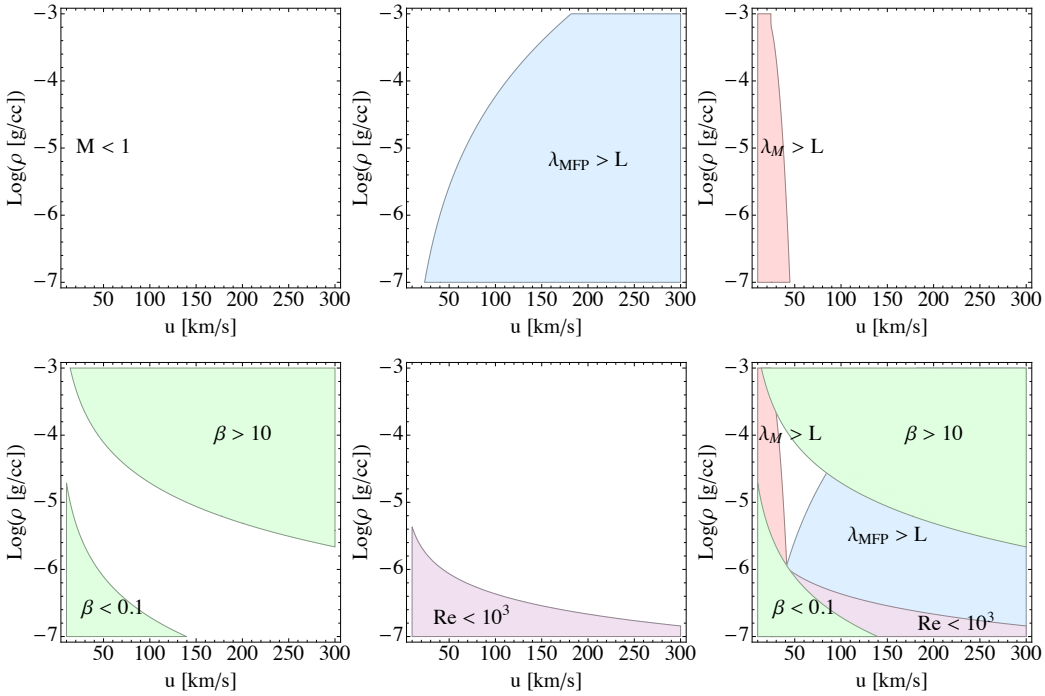

Figure 4.12: Experimental criteria region plots for $T_e = 1.6\,\mathrm{eV}$ and $B = 7\,\mathrm{T}$.

So if the allowed region shrank, did that mean we were less likely to have a well-scaled experiment when only using one drive beam? Not necessarily. Figure 4.13 shows the trajectories of isothermal rarefactions across experimental criteria region plots. Conceptually, these plots are identical to Figure 4.9; here the individual constraint plots have been omitted and only the plots with all five constraints are shown. Although the 6-eV case has the largest allowable region in $\rho - u$ space, a 6-eV isothermal rarefaction does not come close to crossing it. The 1.6-eV isothermal rarefaction just touches the allowable region; it crosses directly from "ion-ion MFP too long to allow a shock" to "β_{ram} too low."

This explains the accretion shock visible light results: as soon as the experiment was able to create a shock, the flow was too dense for the field to affect it. As was seen in Figure 4.5, the magnetic field had no appreciable effect on the shock structures that are observable by visible light imaging.

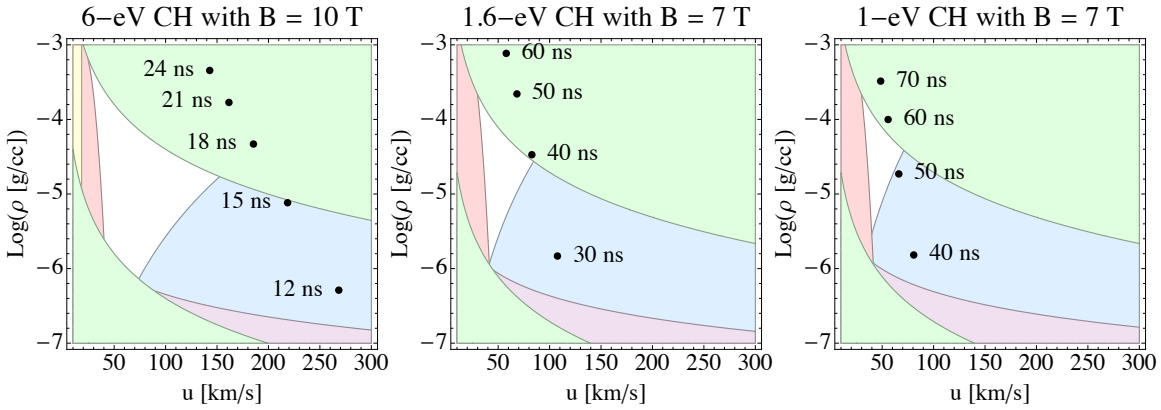

Figure 4.13: Comparisons of isothermal rarefaction trajectories across criteria region plots. For readability, region labels have been omitted but the color coding of Figure 4.11 and 4.12 applies here.

Finally, for comparison's sake I included a 1-eV case in Figure 4.13, although that does not correspond to any experiment shot. The 1-eV does indeed cross into the allowable space, but only stays there for about 5 ns.

This finding has serious implications for the entire field of magnetized flowing

plasma experiments. I devised my scaling requirements specifically for the accretion shock experiment, but *any* magnetized shock experiment would use both my $\lambda_{\rm MFP} < L$ and my $0.1 < \beta_{\rm ram} < 10$ constraints. The former is required to have a shock at all and the later is required to have a field strong enough to do something observable to that shock; these are very general requirements. As seen in Figure 4.13, together two requirements block off much of the ρ–u space. Even if an isothermal rarefaction crosses its allowed area, it will not stay there very long. There are only two ways out of this predicament: increase the imposed field strength or use some other type of incoming jet; both of these are discussed in Chapter VI.

Table 4.3 revisits Table 2.4 from Chapter II, comparing the accretion shock system, the 10-eV experiment with an imposed 10-T field, and the actual 1.6-eV experiment with an imposed 7-T field. The actual experiment produced $\beta_{\rm ram} = 10$, which is equivalent to an accreting young star with $B = 325\,{\rm G}$. As discussed in Chapter II, this is below the expected range of magnetic fields in T Tauri stars (usually one to several kiloGauss), but within the range of expected magnetic fields for Herbig Ae/Be stars (less than 400 Gauss).

4.5 Conclusions

I made the following conclusions about the accretion shock experiment:

1. Visible light images of the accretion shock experiment show a jet emerging, making contact with the impact surface around 43 ns, and a bright volume of shocked plasma forming. Lineouts of the intensity confirm that a shock is present and has grown to a height of 1.2 mm above the impact surface by 63 ns.

2. Based on a simple scaling law, $T \propto I^{2/3}$, if jets driven by seven full-power beams have $T_e = 6 \pm 1\,{\rm eV}$, then jets driven by one full-power beam would have $T_e = 1.6 \pm 0.4\,{\rm eV}$. Comparisons of colliding jet visible light images and accretion

Parameter	Unit	Accreting Star	10-eV Scoped Experiment	Actual Experiment
Mass density, ρ	$\mathrm{g\,cm^{-3}}$	2×10^{-11}	10^{-5}	3×10^{-5}
Average atomic number	-	1.1	6.5	6.5
Average mass number	-	1.3	3.5	3.5
Average ionization	-	0.7	2.4	0.5
Electron density, n_e	$\mathrm{cm^{-3}}$	7×10^{12}	2×10^{18}	1.4×10^{16}
Electron temperature, T_e	eV	1	10	1.6
Velocity, u	$\mathrm{km\,s^{-1}}$	450	100	80
Magnetic field strength, B	G	1000	10^5	7×10^4
Post-shock temperature, T_s	eV	300	40	20
Length scale, L	cm	10^9	0.1	0.1
Ion collisional MFP, $\lambda_{\mathrm{MFP,i}}$	cm	2×10^6	0.02	0.14
Magnetic diffusion length, ℓ_M	cm	200	0.03	0.04
Mach number, $\mathcal{M}$	-	30	4	10
Collisionality, $\lambda_{\mathrm{MFP,i}}/L$	-	0.002	0.2	1.4
Magnetic diffusion length ratio, λ_M/L	-	2×10^{-7}	0.3	0.4
Ram Plasma Beta, β_{ram}	-	1.0	2.5	10
Reynolds number, Re	-	10^{10}	3×10^4	7×10^4

Table 4.3: Comparing the accretion shock system, the original 6-eV experiment with an imposed 10-T field, and the actual 1.6-eV experiment with an imposed 7-T field.

shock visible light images corrobarate this.

3. Visible light images confirm that shocks do form when the ion-ion mean free path falls below the length scale of the system. For the colliding jet experiments from April 2012, this is predicted to occur at 18 ns; visible light images show a shock forming shortly before 20 ns. For the accretion shock experiments, this is predicted around 40 ns; a shock may be evident in the 43-ns image but cannot be distinguished from glow from the impact surface.

4. As shot, the experiment had $\beta_{\mathrm{ram}} \approx 10$, which is above the $\beta_{\mathrm{ram}} \approx 1$ regime we were aiming for. Instead of scaling a young star with $B = 1000\,\mathrm{G}$, our experiment was equivalent to a young star with $B = 325\,\mathrm{G}$.

5. No difference in evolution or morphology was seen in the magnetic-field time

series versus the no-field time series. This is attributed to the magnetic field being too low to effect morphology. There may be subtle differences in structure, but as proton radiography failed it is difficult to say.

6. No isothermal jet will ever be acceptable for a magnetized shock experiment when the imposed field is on the order of $B \approx 10\,\mathrm{T}$. The low temperature required to bring down density and velocity to achieve $\beta_{\mathrm{ram}} \approx 1$ make shock formation impossible.

CHAPTER V

Proton Radiography

Proton radiography is analogous to x-ray radiography, with which most people are familiar (dental x-rays, etc.). In x-ray radiography, x-rays pass through a subject and strike a piece of film. When the film is developed, a density-based image of the subject emerges.

In proton radiography, a stream of energetic protons pass through a subject and strike a collector, in our case a thin piece of a type of plastic. Like x-rays, protons are absorbed by dense materials, but as charged particles, protons are also deflected by electro-magnetic fields. When the plastic, which is analogous to the x-ray film, is developed, an image affected by both density and field-strength emerges.

Our experimental team intended to use proton radiography to study magnetic field structures in the scaled accretion shock. Astrophysical simulations have found gross distortions in magnetic field lines surrounding accretion shocks. Figure 5.1 shows the simulation results of *Orlando et al.* (2010); notice how the laterally expanding accretion shock is sweeping magnetic field lines before it (the field was initially straight up and down). We hoped our scaled accretion shock would produce a similar distortion in the field and proton radiography is ideal for capturing such concentrations in field strength.

Section 5.1 presents the background on the type of proton radiography used, a

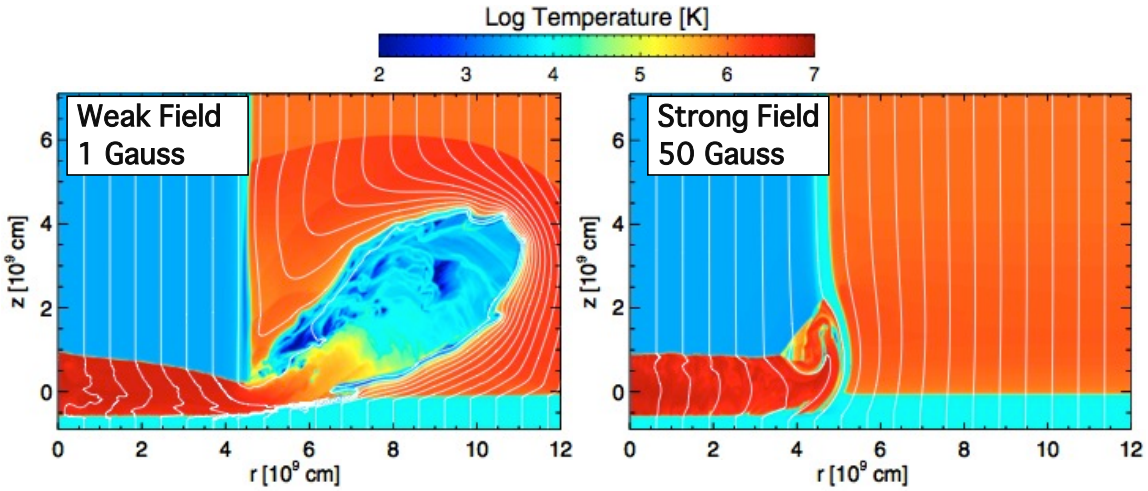

Figure 5.1: Simulation results of *Orlando et al.* (2010). In the weak field case, the (white) magnetic field lines are pushed in front of the accretion shock as it "splashes" out. (This figure was previously used as Figure 2.4 in Chapter II.)

laser-imploded D^3He backlighter paired with CR-39. Although we were successful using proton radiography on a related experiment, the multi-jet experiment, we encountered multiple difficulties when applying it to the accretion shock experiment. Section 5.2 discusses the multi-jet experiment and the associated proton radiography data. I was the graduate student PI for the multi-jet experiment in 2013 but chose to go in a different direction for my thesis work. The multi-jet data are included here to aid in understanding the accretion shock proton radiography data.

Section 5.3 discusses the proton radiography data obtained for the accretion shock experiment. Section 5.4 discusses the difficulties encountered: for the May 2014 shot day the protons were deflected away from the CR-39 and for the May 2015 shot day the proton backlighter was improperly illuminated and proton counts were an order of magnitude lower than expected. Section 5.5 presents my conclusions.

5.1 Proton Radiography Background

5.1.1 Proton generation

This project relied on a monoenergetic proton backlighter developed by *Séguin et al.* (2003) and *Li et al.* (2006). A spherical glass (SiO_2) capsule with a diameter of 427 μm and a shell thickness of 2 μm is filled with deuterium-helium-3 (D^3He) gas at nominal pressures of 12 atm (^3He) and 6 atm (D_2).

When the capsule is subjected to direct laser irradiation, the shell ablates away, driving a shock wave through the capsule. The implosion produces protons via the following fission processes:

$$D + D \rightarrow T\ [1.01\,\mathrm{MeV}] + p\ [3.02\,\mathrm{MeV}], \text{ and} \tag{5.1}$$

$$D +^3 He \rightarrow \alpha\ [3.6\,\mathrm{MeV}] + p\ [14.7\,\mathrm{MeV}]. \tag{5.2}$$

These proton populations are referred to as the 3-MeV DD protons and the 14-MeV D^3He protons (*Séguin et al.*, 2003).

The velocity of the protons is

$$u_p = c\sqrt{1 - \left(\frac{1}{1 + \frac{E_p}{E_o}}\right)^2}, \tag{5.3}$$

where E_p is the energy of the proton and E_o is the rest mass of the proton in energy units. The 3-MeV DD protons have a velocity of $2.4 \times 10^9\,\mathrm{cm\,s^{-1}}$ ($0.08c$) and pass through the experiment (roughly 3 mm across) within 0.1 ns. The 14-MeV D^3He protons have a velocity of $5.3 \times 10^9\,\mathrm{cm\,s^{-1}}$ ($0.18c$) and pass through the experiment within 0.06 ns.

5.1.2 Proton detection

The protons are detected with CR-39, a clear plastic (chemical composition $C_{12}H_{18}O_7$) whose long polymer chains are damaged by the bombarding protons. The CR-39 is later etched in NaOH. Because the damaged areas are eaten away by the NaOH faster than the intact areas, an images of proton irradiance emerges.

When protons pass through CR-39, they deposit their energy in a highly non-linear manner, depositing very little until the end of their flight, and then depositing all their energy at once.[1] This means that the incoming energy of a proton determines its fate. If its energy is high enough, it will pass through the CR-39 unscathed; CR-39 is only 100% efficient at detecting protons in the 0.5–6 MeV range. Otherwise, it will deposit the bulk of its energy, and thus cause most of its damage, at a depth specific to its incoming energy. When the researcher etches the CR-39, the exposure time to the NaOH determines what level of proton damage are left on the surface. By adjusting NAOH exposure time, the researcher can ensure that only protons of a specific energy are seen in the final developed image. Likewise, if the protons above 6 MeV are of interest, the experimenter can place a filter before the CR-39 to bring the proton energy down to something that can be detected by CR-39 (*Séguin et al.*, 2003).

For this project, a stack of 1) 75 μm tantalum; 2) 1500 μm CR-39; 3) 50 μm aluminium; and 4) 1500 μm CR-39 was placed in a Wedge Range Filter, a target chamber apparatus for holding the CR-39.[2]

Typically, the proton backlighter is placed 1 cm from the subject and the CR-39 is placed $\sim$ 30 cm on the other side of the subject, giving a magnification of $\sim 30\times$. As the sheets of CR-39 are 10 cm across, this provides a field of view roughly 3 mm

[1] This always reminds me of the Hemingway quote on going bankrupt: "Two ways. Gradually, then suddenly."

[2] The "wedge" in the name refers to the wedge-shaped filters that are often used for proton spectronomy, but no wedge-shaped filters were used for this project.

across. To obtain a wider field of view, the CR-39 can be brought closer to TCC; 20 cm from TCC is the closest possible, giving a field of view 5 mm across.

5.2 Multi-Jet Experiment

5.2.1 Motivation

Chronologically, the multi-jet experiment falls between the collimated jet work of Chapter III and the accretion shock work of Chapter IV and this chapter. It represents a road not taken; our collaboration considered pursuing a laser-created rotating plasma disk and chose to go a different direction after this day of experiments.

The idea for creating a rotating plasma disk with a "twisted wagon wheel" was laid out in *Ryutov* (2011). As sketched in Figure 5.2, half a dozen or more equally spaced jets would be launched inward (the "wagon wheel" part of the design), but they would each be aimed slightly off-center (the "twisted" part of the design). Thus, the system would have some overall angular momentum and rotation about the central axis would be expected.

Additionally, *Ryutov* intended to impose an external cusp magnetic field on the experiment. A cusp field, see Figure 5.2, uses two current loops in opposite directions to create a field that points in radially, then points outward along the central axis. According to *Ryutov*, the plasma jets would become coupled with the field when they were launched at the edge of the experiment, then drag the field to the center, where it would effect the creation of a rotating plasma disk.

5.2.2 Configuration

The multi-jet experiment was conceived as a stepping stone towards the configuration seen in Figure 5.2. Instead of a whole wagon wheel of jets, we designed a target with only three, which could be shot individually or in some combination, using the

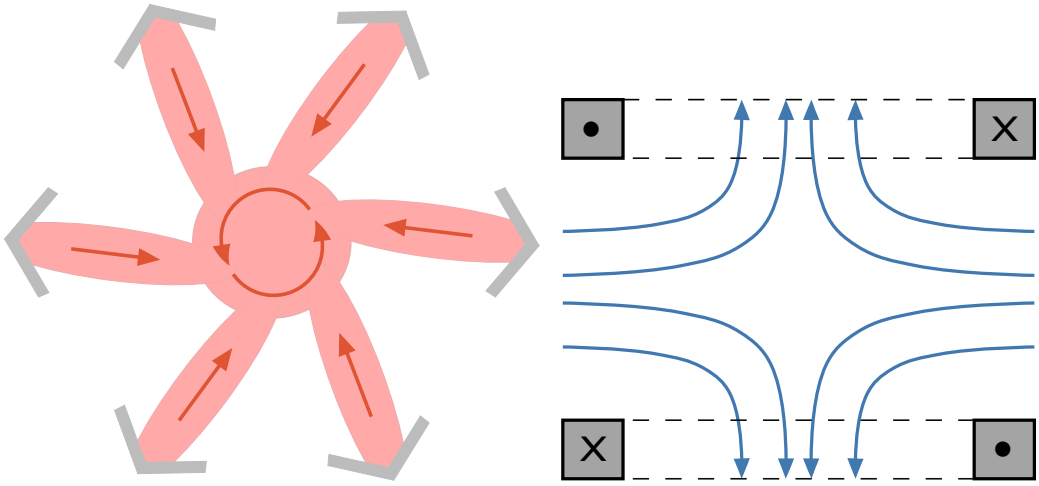

Figure 5.2: Schematic for creating a rotating plasma disk. Left: Each colliding jet is aimed slightly off-center, giving the system overall angular momentum. Right: Two current loops (shown in cross section) create a cusp magnetic field (blue).

jet-creation method tested in April 2012 and discussed in Chapter III. Consistent with the goal of eventually creating a rotating disk, we imposed a cusp field on this experiment.

Figure 5.3 shows the multi-jet experimental scheme. The three cones, which we referred to as "A," "B," and "C," were positioned 4 mm from target chamber center and were separated by 45°. (That is, A and C were 90° apart and B was halfway in between.). The jets were launched with the rear-irradiation method tested in April 2012 and discussed in Chapter III. The plane of the jets was positioned at the mid-plane of the cusp field, "sandwiched" between the two current coils. A proton-generating backlighter was placed 1 cm below the experiment; a 10 cm × 10 cm piece of CR-39 was positioned 30 cm above the experiment, giving a 3 mm × 3 mm field of view. Table 5.1 lists all the vital statistics for the experiment.

5.2.3 Results

On the August 2013 day of experiments dedicated to the multi-jet configuration, we attempted to use proton radiography on seven shots. For six of those shots,

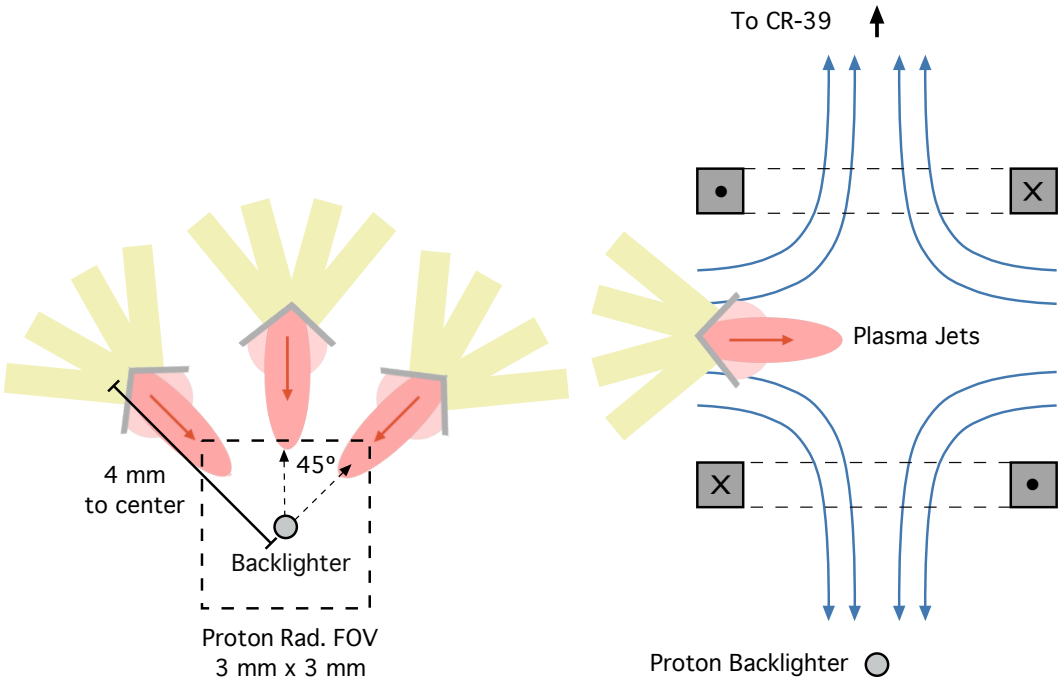

Figure 5.3: Schematic for the multi-jet experiment. Left: A top-down view of the three colliding jets. For clarity, the current coils and proton backlighter have been omitted. Right: A side-on view of the experiment. For clarity, only one jet has been included.

proton radiography was successful, five one-jet shots and one two-jet shot. (We were intending to work towards a three-jet shot and did not get there.) Those proton radiography data were seen in Figure 5.4. These images are from the lower layer of CR-39 in the module which records the 3 MeV protons, as that layer consistently showed a brighter image for this shot day.

Several patterns are evident in the images. First, the three shots for which no magnetic field was imposed, Shots 70673, 70674, and 70681, have a smooth background, while the three shots where a 4-T cusp field was imposed have a wrinkled pattern, almost like a cloth were pinched at the center of the field of view. Second, at least four of the shots show a clear bubble moving into the field of view. These bubbles are easiest to see in the no-field shots, but they also appear, albeit somewhat disrupted, in the cusp-field shots. These bubbles seen on the proton radiographs represent the leading edges of expanding jet rarefactions; both the bubbles and as-

Target	
Material	CH
Solid density	$1.18\,\mathrm{g\,cm^{-3}}$
Cone opening angle	160°
Cone diameter	2 mm
Cone thickness	$100\,\mu$m
Distance to TCC	4 mm
Spacing between cones	45°
Drive Beams	
Drive beam wavelength	351 nm (3ω)
Number beams	4 per cone
Total drive energy	1800 J
Drive beam shape	1 ns, square
Drive beam radius	$352\,\mu$m (SG4)
Drive irradiance	$5 \times 10^{14}\,\mathrm{W\,cm^{-2}}$
Proton Backlighter Beams	
BL beam wavelength	351 nm (3ω)
Number beams	16
Total drive energy	7200 J
BL beam shape	1 ns, square
BL beam focus	1.81 mm

Table 5.1: Experimental parameters for the multi-jet experiment of August 15, 2013.

sociated jet directions have been labeled in Figure 5.4. Third, the orientation of the proton radiograph appears to have been wrong in several shots. We know for certain which cone was fired; this information is stored in the OMEGA online data system, so there is no doubt that Shots 70672 and 70673, for example, fired the same lasers and launched the same jets. That the jets appear to come from the opposite directions in the two radiographs is undoubtedly due to the CR-39 being inadvertently rotated.

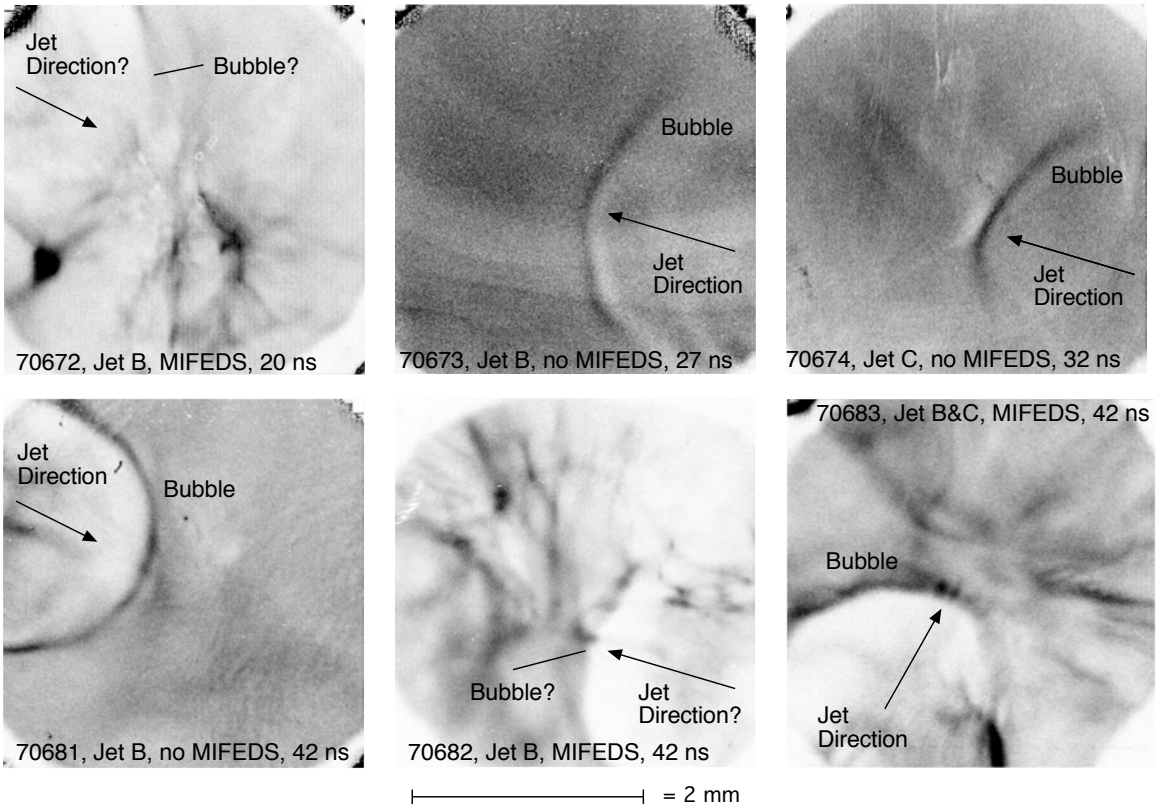

Figure 5.4: Proton radiography data from August 2013. These images show the lower layer of CR-39, which records 3 MeV protons.

5.3 Accretion Shock Experiment

5.3.1 Configuration

The motivations and experimental set-up for the accretion shock experiment have been discussed extensively in Chapters II and IV.

5.3.2 Results

Despite conducting proton radiography on two full days of shots, we saw the distinctive bubble pattern discussed in Section 5.2 only once: on Shot 77255 from May 2015. Since this is the only case of accretion shock proton radiography data with recognizable plasma or field features, it bears its own discussion. Figure 5.5 shows the data of this shot alongside that of a control shot.

The jet in Shot 77254 was launched with seven drive beams and the proton backlighter was fired 10 ns after drive. The visible light imager was gated to 13–16 ns. Figure 5.5 shows both proton radiography and visible light data for the control shot (Shot 77254, top row) and the jet shot (Shot 77255, bottom row). When the jet is seen barely touching the impact surface in the visible light image, there are three bubbles evident in the proton radiography image. The first is the primary bubble made by in the incoming jet, while the second and third are made by blow-off from both sides of the wall. The field of view was at the edge of the CR-39, so the opposite wall and its blow-offs were not evident in the proton radiography image.[3]

These bubbles are remnants of the magnetic field transferred to the plasma while the laser is on. During the laser pulse, some portion of the laser magnetic field propagates into the newly formed plasma, where it is convected to the edge of the plasma. This local field appears at the edge of the expanding cloud of plasma as a

[3]The field of view was not centered on the CR-39 because we knew that we would be using different magnetic field strengths on shot day and needed to allow for differing proton deflections, see Section 5.4.

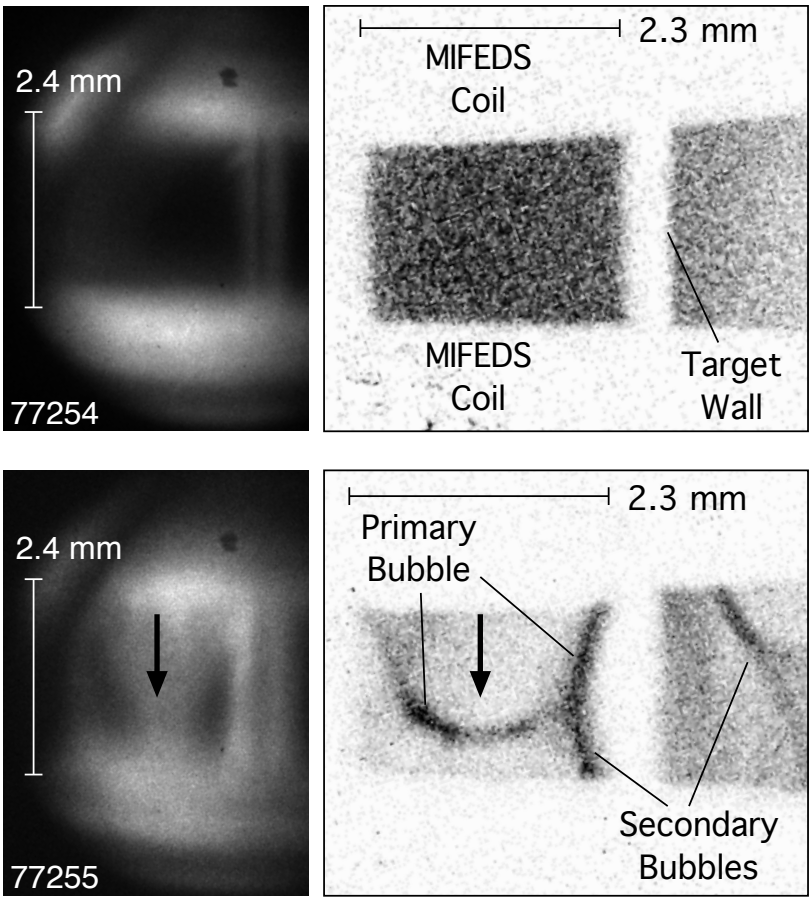

Figure 5.5: Comparing successful proton radiography data to a control shot. Above: The visible light image (left) and 14-MeV proton radiograph (right) for Shot 77254, a control shot. Below: visible light image (left) and 14-MeV proton radiograph (right) for Shot 77255, a seven-beam shot. The black arrows indicate jet direction.

distinct line in proton radiographs (*Eliezer*, 2002; *Li et al.*, 2007).

Once the laser turns off, the magnetic field at the bubble surface begins to diffuse away. If the time scale of interest is τ, the amount of time elapsed since the laser turned off, then the magnetic diffusion length by simple unit analysis is $\ell_m = \sqrt{\tau \nu_M}$, where ν_M is the magnetic diffusivity. As seen in Chapter II,

$$\nu_M = \frac{c^2 \eta_\perp}{4\pi}, \tag{5.4}$$

where c is the speed of light, and $\eta_\perp$ is the transverse Spitzer resistivity, defined in

Equation 2.12.[4]

Table 5.2 lists the shot configurations from August 2013, May 2014 and May 2015, whether radiographic bubbles were observed, and, for those configurations where they were absent, why. For the 1-beam shots, plasma bubbles are never seen. For the 4-beam shots, plasma bubbles are seen at all timings, 27–42 ns. For the 7-beam shots, a plasma bubble is seen in the 10-ns shot, but not the later 30-ns and 70-ns shots. Why are bubbles absent from so many shots? They must have either 1) diffused away, 2) moved out of the field of view, or 3) ceased to exist because they struck a solid surface.

The one accretion shock shot to show a plasma bubble is the 7-beam shot at 10 ns. At 10 ns, the plasma bubble has nearly reached the impact surface. Thus, it not surprising that no plasma bubbles are evident at later times, 30 ns and 70 ns; the bubbles have moved out of the field of view or collided with the impact surface or walls of the target. Similarly, the late-time 1-beams shots do not show plasma bubbles either.

However, the 20-ns 1-beam shot ought to be similar to the 10-ns 7-beam shot; based on the scaling arguments of Chapter IV, a 10-ns 7-beam shot would be equivalent to a 19-ns 1-beam shot. What became of the plasma bubble? Table 5.2 shows the length the magnetic field has diffused based on ℓ_m, where τ is the length of time elapsed since the laser was fired. By 20 ns, the magnetic field in the 1-beam experiment has diffused 0.3 mm and the bubble has disappeared. Not only has more time elapsed in the 1-beam shot, but the field will diffuse more quickly in a colder plasma because $\eta_\perp \propto T_e^{-2/3}$.

[4]There is one crucial difference between this discussion and that of Chapter II. There the plasma of interest was the heated post-shock plasma; here the interest is in pre-shock plasma.

Drive	Timing	Bubbles?	Reason	ℓ_m
1 beam	20 ns	✗	Diffusion	2.5 mm
1 beam	40 ns	✗	Out of range	-
1 beam	60 ns	✗	Out of range	-
4 beams	27 ns	✓	-	1.4 mm
4 beams	32 ns	✓	-	1.4 mm
4 beams	42 ns	✓	-	1.5 mm
7 beams	10 ns	✓	-	0.9 mm
7 beams	30 ns	✗	Out of range	-
7 beams	70 ns	✗	Out of range	-

Table 5.2: Plasma bubbles in proton radiograph data.

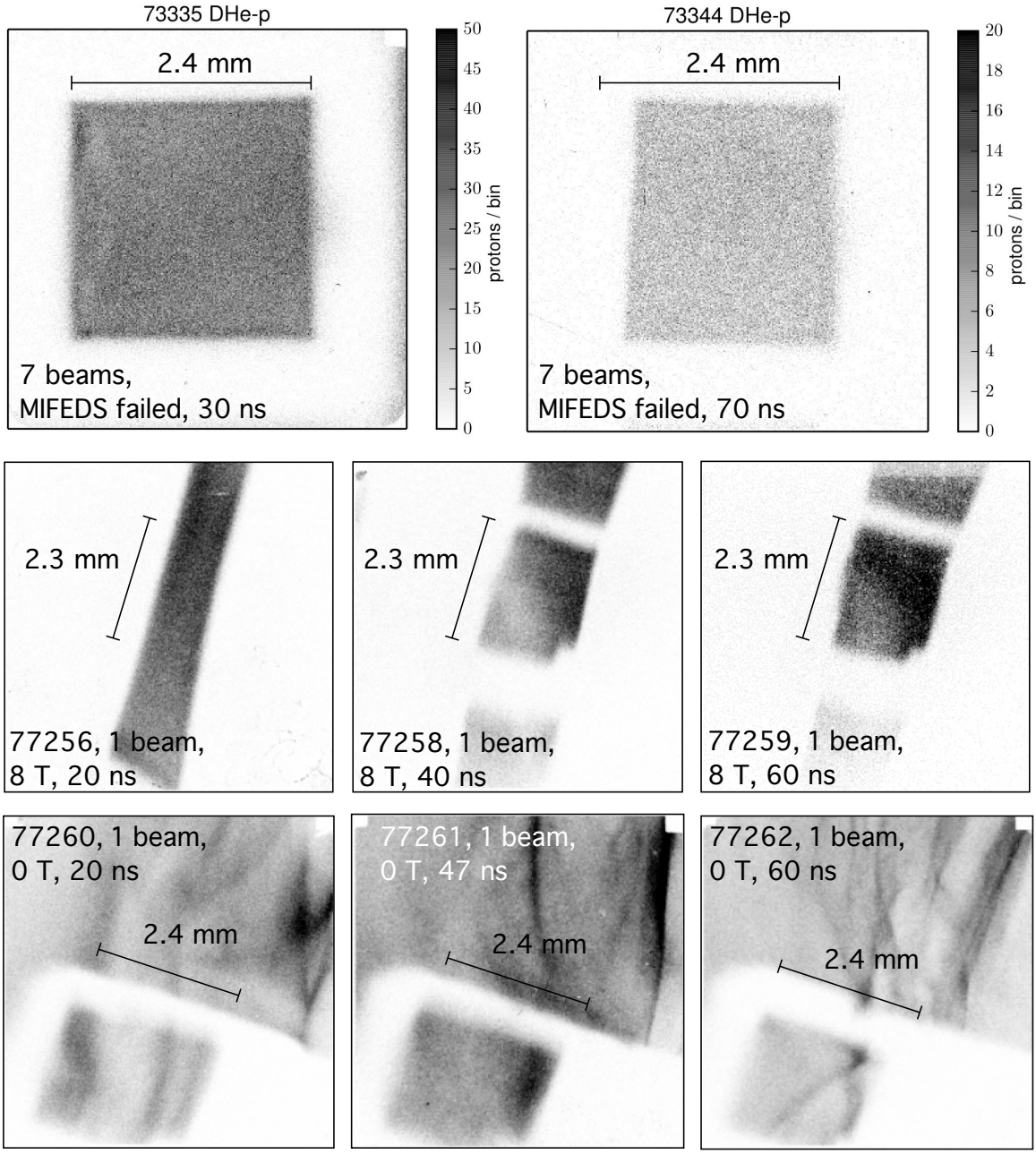

Figure 5.6: Inconclusive proton radiography data for the accretion shock experiment. The top two shots are from 2014; the rest are from 2015.

5.4 Difficulties Encountered

5.4.1 Proton Deflection Issues

5.4.1.1 Issue

Many of the proton radiographs obtained in May 2014 were extremely odd and riddled with strange shapes, see Figure 5.7. The no-field proton radiographs showed a thick white frame surrounding a flat gray background. The frame is the target; the walls, roof and impact surface create the appearance of a frame in the proton radiograph. The uniform gray inside the frame is due to the lack an imposed magnetic field. In the magnetic-field shots, the frame itself is either gone or distorted and other odd looking structures appear.

This, I have concluded, is due to proton deflection. The protons are being diverted by the magnetic field; those that pased through the experiment did not arrive at the CR-39. The protons that *did* arrive at the CR-39 did not pass through the experiment, but instead pass off to its side. The images in the proton radiographs taken with the field on are of a non-experimental part of the target.

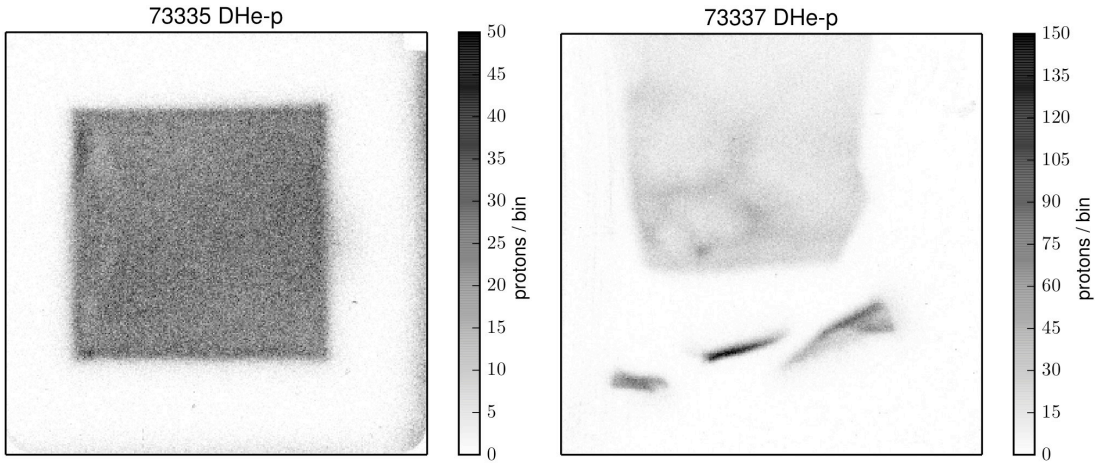

Figure 5.7: Comparing no-field and 7-T proton radiographs. May 2014 proton radiography data from a no-field shot, Shot 73335 (left), and a 7 T shot, Shot 73337 (right).

5.4.1.2 Deflection Calculation

If a charged particle travels through a magnetic field, it will experience a Lorentz force, which, in CGS units, is

$$\mathbf{F} = q\frac{\mathbf{v}}{c} \times \mathbf{B} = -\frac{qv_x B_z}{c}\hat{\mathbf{y}}, \tag{5.5}$$

where q is the charge, v_x is the velocity in the x-direction, B_z is the magnetic field in the z-direction, and c is the speed of light. Therefore the acceleration is

$$\mathbf{a} = -\frac{qv_x B_z}{mc}\hat{\mathbf{y}}, \tag{5.6}$$

where m is the particle mass. Therefore we can find the total deflection from the original path, Δy, by integrating for any arbitrary B_z and any two points, x_1 and x_2, see Figure 5.8. The velocity during its flight will be

$$v_y(t) = \int_0^t a_y(t)dt = \int_0^t \frac{B_z(t)}{mc}dt, \tag{5.7}$$

and the deflection will be

$$\Delta y(t) = \int_0^t v_y(t)dt. \tag{5.8}$$

The experiment had a solenoidal field. The magnetic field in the z-direction as a function of x was

$$B_z(x) = \frac{B_0}{0.715\pi\sqrt{Q}}\left[E(m)\frac{1-\alpha^2-\beta^2}{Q-4\alpha} + K(m)\right], \tag{5.9}$$

where $E(m)$ and $K(m)$ are complete elliptic integrals of the second and first kind, respectively, and

$$\alpha = x/R, \tag{5.10}$$

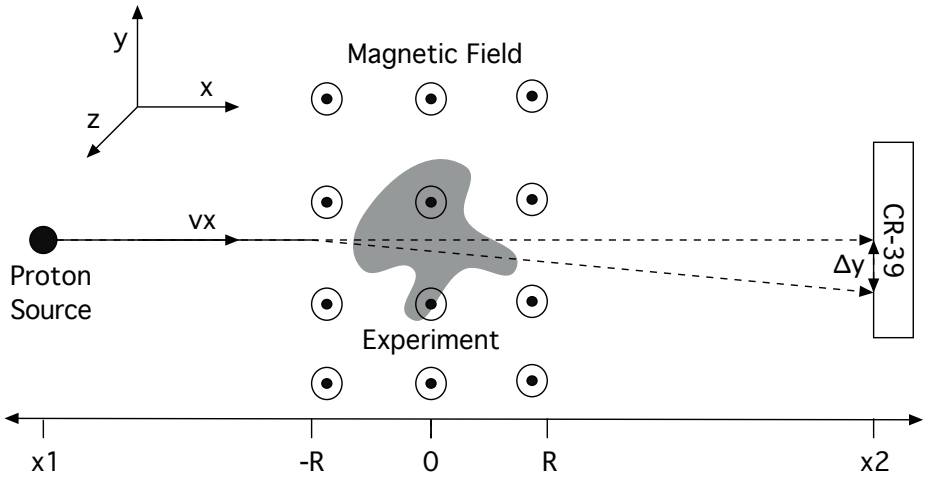

Figure 5.8: Proton deflection diagram. The proton is emitted at x_1, flies through the set-up with $\hat{x}$ velocity v_x, and is absorbed at x_2 by the CR-39.

$$\beta = h/R, \tag{5.11}$$

$$Q = (1+\alpha)^2 + \beta^2, \text{ and} \tag{5.12}$$

$$m = 4\alpha/Q. \tag{5.13}$$

Figure 5.9 shows the B-field normalized to arbitrary units, such that $B = 1$ at $x = 0$, for our experiment, where the protons are generated at $x_1 = -1\,\text{cm}$ and collected at $x_2 = 27\,\text{cm}$.

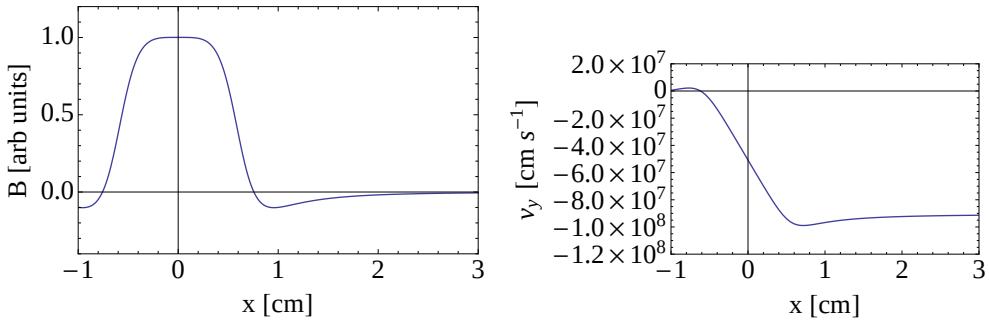

Figure 5.9: [Magnetic field strength and deflected velocity vs. position. Left: the field strength along the x-axis between two coils of current. Right: the deflection velocity. Note that the x-axis only goes to $x = 3\,\text{cm}$ even though the protons are collected at 27 cm.

We expect the deflection on the CR-39 to be $\Delta y_{\text{tot}} = -1.16 B_T\,\text{cm}$, where B_T

is the field strength in Teslas. Or roughly speaking, we expect the protons to be diverted one centimeter per Tesla of field strength. Applying this to Figure 5.7, we would expect Shot 73335 to have a shift of 0 cm, which is what we appear to see. Shot 73337 would be shifted by 8.1 cm, so the window seen in Shot 73335 that spans roughly -2.5 cm to 2.5 cm would be shifted to $+5.6$ cm to $+10.6$ cm, completely off the CR-39. This is consistent with the earlier statement that the image captured for Shot 73337 shows the wires connecting the MIFEDS loops.

5.4.1.3 Solving the Problem

To solve this problem for the May 2015 shot day, we offset the proton backlighter from the line of sight. With this configuration, rather than deflecting the protons off the CR-39, the field deflected them onto it.

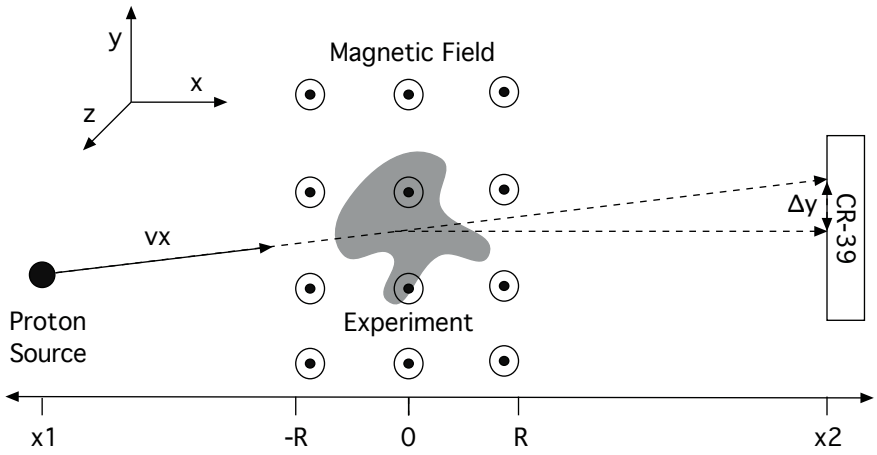

Figure 5.10: Offsetting the proton backlighter solved the deflection problem by making the protons deflected *onto* the CR-39.

5.4.2 Backlighter Focus Issues

In May 2015, we consistently got low neutron counts from the Nuclear Diagnostic Inserter (NDI), with an average of 8×10^7 neutrons per shot, compared to an average of 5×10^8 neutrons per shot in May 2014. During the October 2015 day (which was largely devoted to another campaign), we discovered during conversations with

OMEGA that we had had the backlighter beams focused incorrectly. We had selected a focus of 0.00 mm (that is, best focus) while we should have set the focus to 1.81 mm. That would de-focus the backlighter beams such that they evenly irradiate the backlighter capsule. At best focus, the backlighter beams act as pin pricks, cracking the capsule before it implodes. Fusion is disrupted, and the proton count drops.

5.5 Conclusions

I made the following conclusions about the accretion shock experiment:

1. At early times, plasma jets appear in proton radiography as "bubbles." These are readily visible with or without an imposed magnetic field, and actually appear crisper without a field.

2. With time, the magnetic field that causes the proton radiograph bubbles will diffuse away. The magnetic diffusion length is a function of time and temperature; later times and colder temperatures will show more diffusion. For the data collected in this project, bubbles are still evident when $\ell_m = 0.1mm$, but not when $\ell_m = 0.3mm$.

3. Only one accretion shock experiment, a seven-beam shot with proton radiography 10 ns after drive, shows the distinctive bubble pattern. This shot reveals a bubble caused by the incoming plasma jet, but also secondary bubbles caused by blow-off coming from the wall. We must conclude that the presence of the walls affects the physics of the accretion shock experiment.

CHAPTER VI

Conclusion

6.1 Accomplishments

This thesis captures seven years of work on laser-driven plasma experiments, including four shot days on the OMEGA laser. As the graduate student principal investigator, I was responsible for each shot day from start to finish. I determined the physical questions driving each investigation, designed the experiments, worked with engineers at the University of Michigan to build the targets, oversaw the shot day in the control room at OMEGA, and analyzed the data that resulted. I worked under the supervision and guidance of Carolyn Kuranz and Paul Drake, but the work presented in this thesis is mine except where explicitly stated otherwise.

The idea of a laboratory astrophysics experiment aimed at creating a scaled accretion shock was the result of discussions I had with Patrick Hartigan (Rice University) in early 2011. (Dr. Hartigan was my undergraduate advisor; my undergraduate thesis was the jets that emanate from young star systems.) A collaboration between the University of Michigan and Rice University became feasible in the late 2013/early 2014 and it was then that we began to plan the accretion shock experiment in earnest. By that point, I had gained two shot days worth of experience on OMEGA and had worked with all of the systems and diagnostics that would be needed for the accretion shock system, including launching collimated plasma jets, imposing magnetic fields on

experiments, using the 2-D visible light imager, and using proton D^3He radiography.

This research encountered numerous experimental problems: both 4ω Thomson scattering and proton radiography failed repeatedly. These experiences provided me with life lessons on doing research, but unfortunately they did not provide me with data. The question that drove the investigation, "How does magnetic field strength affect accretion shock structure and evolution?," is yet unanswered. As discussed in Chapter IV, the actual experiment had $\beta_{\text{ram}} \approx 10$. At such a β_{ram}, the magnetic field is not high enough to produce differences in gross structure.[1] There may have been nuanced differences due to the imposed field, but as proton radiography failed these went unrecorded.

Despite this, I believe this thesis project is a meaningful contribution to the field of laboratory astrophysics. The experiences gained in this research project have advanced other projects at CLEAR, particularly projects in the magnetized flowing plasma group. I was also able to complete many of the smaller goals I set as part of the overarching accretion shock endeavor. Listed below are what I consider my major accomplishments:

1. I scaled accretion shocks observed in star formation to a laboratory experiments and in doing so developed a visual process for scaling laboratory astrophysics experiments.

2. I successfully tested a method for creating collimated plasma jets and found them to behave like isothermal rarefactions.

3. I found a way to overcome probe beam heating in Thomson scattering by inferring the pre-heating temperature of the jets from their mass density profile.

4. Despite repeated failures involving key diagnostics, I proved that a scaled accretion shock was created in the laboratory. The plasma parameters of this scaled

[1] β_{ram} is the ratio of plasma pressure to magnetic pressure, see Chapter II.

shock would correspond to a young accreting star with $B = 325\,\mathrm{G}$.

5. I found that shocks form when the ion-ion mean-free-path falls below the scale length of the system.

6.1.1 Scaling process

For a laboratory astrophysics experiment to be valid, it is not enough to superficially resemble the astrophysical phenomenon in question. It must be well-scaled, which requires that the relevant dimensionless numbers be in the same regime for both the astrophysical phenomenon and the experiment. Using dimensionless numbers to scale experiments is a well-established approach, but the graphical approach I used is, as far as I know, unique in laboratory astrophysics. I created region plots in plasma parameter space for each dimensionless number constraint; each plot showed the area where the constraint was and was not met. By graphing these regions simultaneously, I was able to visually represent the area where all the constraints were satisfied at once. This method allows a researcher to see how an experiment is moving through allowed parameter region with time and to determine for what time range the experiment will be well-scaled. See Chapter II.

6.1.2 Collimated jets

In April 2012 our experimental team tested a method for creating collimated plasma jets on OMEGA by rear-irradiating a thin cone of acrylic. Two-dimensional visible light self-emission images proved that we were successful; the jets were well collimated. We used Thomson scattering for each shot and successfully collected scattered spectra from 12 ns to 18 ns. I analyzed these data to find the mass density profile of the experimental jets and compared it analytically predicted mass density profiles for adiabatic and isothermal rarefactions. There was a clear match between the experimental mass density profile and that of the isothermal rarefaction. There-

fore, I concluded that the jets were behaving like isothermal rarefactions. See Chapter III.

6.1.3 Overcoming Thomson probe heating

If the experimental plasma absorbs some of the Thomson probe beam energy, it can be heated to a temperature well above its initial temperature, corrupting the resulting Thomson scattering data. This occurred during the April 2012 experiments. The measured temperatures are on the order of 50–400 eV; temperatures on the order of 10 eV are typical of rear-irradiated jets. I built a simple steady-state probe-heating model and found that there was good agreement between the temperature predicted by my probe-heating model and the temperatures found from Thomson scattering.

I was, however, able to overcome the probe heating problem with the mass density profile approach described in Section 6.1.2. I compared the experimental mass density profile to analytic predictions of the mass density profile for isothermal rarefactions at varying temperatures. I found that an isothermal rarefaction of $T_e = 6 \pm 1\,\mathrm{eV}$ bounded the mass density data. See Chapter III.

6.1.4 Scaled accretion shock

Young stars are thought to grow via magnetospheric accretion, wherein material from the accretion disk is funneled to the stellar surface along magnetic field lines. To create a scaled version of this system, I drove a plasma jet (the "accreting flow") into a solid block (the "stellar surface") in the presence of a parallel magnetic field (analogous to the local stellar field). The imposed field was intended to resemble the stellar magnetic field which runs perpendicular to the stellar surface where the accretion shocks form. I performed this experiment on two days of shots at OMEGA. Although proton radiography failed on both days (for independent reasons), 2-D visible light imaging was successful.

Visible light images show the jet colliding with the impact surface and a bright shock structure forming. Previous experiments had shown that jets launched with seven full-power beams were isothermal rarefactions with $T_e \approx 6\,\mathrm{eV}$ (see above). The scaling expression, $T_e \propto I^{2/3}$, suggests that the jets used for the accretion shock experiments, which were launched with one beam, would be isothermal rarefactions with $T_e \approx 1.6\,\mathrm{eV}$. Using the density and velocity analytically predicted for a 1.6-eV isothermal rarefaction, I concluded that the scaled accretion I created would be equivalent to a young star with $B \approx 325\,\mathrm{G}$. See Chapter IV.

6.1.5 Shock formation and mean free path

Both of the major experiments presented in this thesis, the collimated jet experiment and the accretion shock experiment, involved collisions and resultant shocks. When designing the accretion shock experiment, one of the scaling arguments I used was the prediction that a shock would not be observed unless the ion-ion mean-free-path was less than the scale length of the experiment. The collimated jet experiment produced jets with $T_e = 6\,\mathrm{eV}$ and collided two jets head-on (that is, 180°). Plotting the $\rho - u$ trajectory of a 6-eV isothermal rarefaction on the mean-free-path region plots developed in Chapter II, a shock ought to form at roughly 18 ns, consistent with visible light images.

The accretion shock experiment drove a single jet into an impact surface perpendicular to the jet. Scaling arguments suggest these jets were isothermal rarefactions with $T_e = 1.6\,\mathrm{eV}$, and the $\rho - u$ trajectory plotting strategy described above predicts that a shock becomes possible for the accretion shock experiment around 40 ns. Again, this is consistent with visible light images. See Chapter IV.

6.2 Future Work

As stated earlier in the Chapter, the driving question for this investigation, "How does magnetic field strength affect accretion shock structure and evolution?," has not been answered. No difference in shock structure was observed between the shots with an imposed field and one without. This section explores why that might be and how it could fixed for future work. In short, the lack of an observed difference for field and no-field shots could be due to the repeated experimental failures, or it could be due scaling problems. If the fault lies with the experimental failures, then repeating the experiment with the problems fixed would yield useful data. However, if the experiment failed to observe a difference between the field and no-field cases due to scaling, then major design changes would be necessary.

6.2.1 Experimental failures

Proton radiography failed for both the May 2014 and the May 2015 shot days. The May 2014 loss was due to protons being deflected off the CR-39, while the May 2015 loss was due to the wrong beam focus being used to implode the backlighter capsule. With both of these failure modes well understood, CLEAR has recently used D^3He proton radiography successfully for another magnetized flowing plasma shot day. In that sense, the problem is solved. However, it is worth considering the proton radiography failures here to avoid similar failures in the future.

Of all the things that went wrong in this thesis project, the hardest to get over is the loss of proton radiography data in May 2014. After we got the data, I calculated the expected path of a proton through my May 2014 experiment and discovered my mistake. The necessary change to that problem was very simple: we moved the proton backlighter 1 mm to avoid the same mistake in May 2015. (In theory, we could have asked to have the beams redirected as late as the night before the shot day, had we known about the problem.) The only lesson that I can takeaway form this is the

importance of doing such calculations in advance, which I would emphasize to future students.

By contrast, I *did* predict my Thomson data for the April 2012 shot day and in doing so caught a critical mistake. When I calculated the Doppler shift and Thomson peak separations, my predicted Doppler shift was nearly zero. Surprised, I ran the same calculation for an experiment published in the literature, *Ross et al.* (2012), and discovered the error I had made in designing my experiment: I had made the velocity and the Thomson scattering k-vector nearly perpendicular when they ought to be parallel. Having discovered this mistake, I reoriented the experiment in the chamber to make the jet velocity parallel to the k-vector (which is determined by the entry point of the probe and the location of the collection telescope and cannot be altered), and redesigned the targets accordingly. This mistake was caught fairly late in the planning process—a portion of the targets had already been partially machined and new ones had to be made with the correct stalk angle. But had this mistake not been caught at all, we would have lost velocity data on shot day.

6.2.2 Scaling issues

Scaling issues are harder to rectify than experimental issues. The validity of this genre of work hinges on getting β_{ram} into the coveted $\beta_{\text{ram}} \approx 1$ regime. There are, obviously, two ways to do that: increase the magnetic field or decrease the incoming jet density and velocity. Both of those are difficult.

OMEGA uses a TIM-based[2] system, MIFEDS, to generate magnetic fields. Thus, the capacitors that power MIFEDS must fit in a fixed volume—and most of the space is already devoted to capacitors and their associated charging system. The Laboratory for Laser Energetics (OMEGA) is currently funding Gennady Fiksel here at the University of Michigan to develop a 30-T, and later a 50-T, version of MIFEDS,

[2]TIMs, or Ten-Inch-Manipulators, are basically portals into the target chamber, see Appendix A.

but until these are completed and qualified, the maximum capability will remain fields on the order of 10 T when an experimental volume several millimeters across is required.

The other way to increase field strength, making the current loop smaller, is unfeasible with this experiment. The target has to fit inside the current loop, so there is a limit to how small the current loop can be made without making target positioning impossible. This is something we already pushed to the limit in designing the May 2014 and May 2015 experiments.

Creating a low-density, low-velocity plasma stream with a laser is likewise difficult. Lasers deposit a lot of energy in a short amount of time; they therefore lend themselves to creating high-velocity jets that do not last very long. Irradiating the rear side of the target creates reservoir of hot plasma which can then expand over a longer period of time, which is why we chose to using rear irradiation instead of front irradiation. This is also why we chose to fall back to one beam (instead of the seven we had previously been using) for the second day of accretion shock experiments. Even so, plasma β_{ram} was on the order of ten. One potential solution would be to use a heater beam, exposing the incoming jet to an additional laser beam that heat it. Then one could have the advantages of a low-temperature isothermal jet (low density, low velocity) with the advantages of higher temperature (easier shock formation due to higher ionization).

There is also work ongoing to find other ways to create low-density, low-velocity plasma streams. The collaboration established for this thesis project (Michigan, Rice, MIT, and LLNL) has grown to include other magnetized flowing plasma projects. One project, which created magnetized bow shocks, developed a new method for creating low-density, low-velocity plasma streams. They launched two jets via rear-irradiation, collided them head-on, then used the expanding plasma from the central collision as the flow of interest. Conceptually, their method was similar to the April 2012 colliding

jet project, except they were looking at the flow emanating from the central collision, not the central collision itself. Perhaps this path forward would get the accretion shock experiment into the $\beta_{\text{ram}} \approx 1$ regime.

6.3 In closing

Despite the difficulties encountered in this thesis project, I still feel astonishingly fortunate. Not every graduate student is permitted to essentially design her own experimental campaign from the ground up and I am grateful for the opportunity to do so. It is bittersweet to walk away from an endeavor just as it seems all the problems are solved and everything is looking up, but I suppose that is the nature of graduate school. It is my hope that these experiments will be continued on in some form; the proton radiography problems are solved and the low-density, low-velocity drives being developed could reduce β_{ram} to something genuinely useful. But regardless of whether this particular experiment continues, I know that CLEAR will continue to do this genre of work and that is gratifying.

APPENDICES

APPENDIX A

Diagnostics

This appendix provides background on OMEGA, including the planning process for a day of OMEGA experiments, called a shot day, and background on the major systems used for this project.

OMEGA provides diagnostic flexibility with its six Ten-Inch Manipulators or TIMs, basically portals into the target chamber that can accept any one of more than 150 different diagnostics. While many OMEGA diagnostics can be placed in any of the six TIMs, some newer diagnostics have only been qualified in one or two. If the researcher wishes to use such a diagnostic—as was the case with my experiments using Thomson scattering—the experiment must be planned around it. In addition to the TIM-based diagnostics, OMEGA has roughly 30 diagnostics built into the target chamber.

Section A.1 explains the process for planning an OMEGA shot day. Section A.2 provides background on the system used to impose magnetic fields on experiments, Magneto-Inertial Fusion Electrical Discharge System or MIFEDS. Section A.3 presents Thomson scattering, a technique which probes parameters such as temperature and density by scattering a probe laser beam off the experimental plasma. Section A.4 explains visible light imaging, which is as straightforward as it sounds,

simply taking a picture of the experiment using self-emitted light.

A.1 Planning an OMEGA Shot Day

A.1.1 12 months out

Planning for an OMEGA shot day begins a year in advance. The research team has a rough idea of what the day will be used for since OMEGA, like all major facilities, allocates time based on proposals. At this point, the particulars need to be hammered out. What are the specific goals of *this* shot day and how do they relate to the campaign as a whole? What will the experimental scheme look like? What major diagnostics or other systems will be needed?

At this point, the research team creates a brief (3 slide) presentation for planning purposes at LLE. OMEGA functions most efficiently if days that use similar diagnostics are grouped together. For example, because Thomson scattering requires a dedicated beam (see Section A.3), it is only done during dedicated $2\omega/4\omega$ Thomson weeks.

Around this time preliminary target design begins. A final design will not be necessary until about three months out, but if the target includes any long-lead items, the CLEAR target fabrication engineer needs to know so that she can source it. (CLEAR is unique in that all of our targets are made in-house; most research programs order them from an outside source.)

Targets are designed in VisRad, a computer-aided design program that has the OMEGA target chamber built into it. VisRad allows the designer to view the target from any point of view in the chamber and has the coordinates of the TIMs and fixed diagnostics built in. VisRad is also used to assign beams to the experiment.

Part of the planning process is completing Shot Request Forms, or SRFs. Every shot has a unique SRF which lays out all the necessary information about targets,

beams, drivers, TIM assignments (which diagnostics are going where), and diagnostic set-up. The OMEGA staff will follow the SRF verbatim, and the SRF will serve as a record of precisely what settings were used on the shot. Work begins on these 4 to 6 months in advance. At this point, there is no need to have an entire shot day's worth of SRFs complete; only one SRF per unique configuration is needed.

As the graduate student PI, much of this work was my responsibility. I helped to determine the goals of each shot day, did the background research necessary to design the experiment (see Chapter II), prepared the 3-page planning presentation for LLE, designed the experiments in VisRad, and completed the SRFs.

A.1.2 3 months out

Three months before the shot day, the experiment is largely designed and the responsibilities shift to coordinating the logistics of the shot day.

At this point, the experimental team submits a proposal, which includes an SRF and associated VisRad for each unique configuration that will be used on shot day. The purpose of the proposal is to allow the facility to identify any problems well in advance. Changes can still be made to the experiment, but they require corresponding with the facility engineers and then resubmitting the proposal.

Target fabrication is completed in this time frame. Engineering drawings of the target are made. Because my targets were machined in-house, I worked closely with our micro-machinist in creating my drawings and made changes based on his suggestions, for example rounding out inside corners to accommodate the size of the drill bit. After the targets are made, they must be measured using the CLEAR metrology system.

As the graduate student PI, I completed VisRads and associated SRFs for each configuration and made engineering drawings. I also metrologized (measured) the resulting targets to ensure that they were built to specification.

A.1.3 2 weeks out

At this point, the logistical details have been hammered out and this time period in the cycle is dedicated to addressing late-breaking problems. Experimental teams are expected to brief LLE staff two weeks before the shot day and again one week before. (These briefs are conducted over the phone with prepared slides.) During this time period, a rough shot sequence is laid out. Generally, it is a good idea to work from basic to complicated configurations and to put off using equipment that is prone to failure until late in the day.

A.1.4 Shot day

Shot days last about twelve hours, spanning two shifts of OMEGA personnel. As the grad student PI, I briefed each shift of OMEGA staff (engineers and technicians) about the experimental goals, configurations that would be shot and diagnostics that would be needed. Although all of the hands-on work is done by OMEGA staff, I was responsible for granting my approval. For example, target are aligned by OMEGA to meet the specifications of the submitted VisRad, but I was expected to approve (or not) the aligned target based on its view in the camera.

OMEGA is remarkably flexible. Changes to a shot can be made up until a few minutes before the shot is fired. This means that the experimental team can decide what the next shot will be based on the last shot's results. As a good shot day only has about a dozen shots, it is crucial to think through the "flow-chart" of what shots will be needed based on early results.

A.2 Imposing Magnetic Fields with MIFEDS

A.2.1 Capabilities

The Magneto-Inertial Fusion Electrical Discharge System (MIFEDS) is a TIM-based electric discharge system used to generate experimental magnetic fields on OMEGA (*Gotchev et al.*, 2009; *Knauer et al.*, 2010). MIFEDS was recently redesigned to be "more user-friendly" while meeting all of its original requirements (*Fiksel et al.*, 2015). Energy is stored in high-voltage capacitors, then discharged through a wire coil when a laser-based trigger is fired, achieving voltages of 10–20 kV. This achieves magnetic fields of 5–15 T extending over several cubic centimeters and lasting for 1 μs = 1000 ns.

As seen in Figure A.1, much of the volume inside the TIM is dedicated to the high voltage (HV) capacitors and their associated charging supply. When MIFEDS is fired, the spark-gap switch connects and the capacitors discharge through the high voltage transmission line leading to the magnetic coil.

The zoomed section shows the magnetic coil itself. Each coil design is unique its experimental configuration. Coils are 3-D printed by LLE (the white plastic seen in Figure A.1), then insulated copper wire is wrapped around them as shown. When MIFEDS is fired, the heat of the current discharge destroys the coil; these are single use items. When the used coils are removed from the target chamber, the plastic part is gone and the wire has been mangled by the intensity of the magnetic field.

A.2.2 Development and Use

As its name would suggest, MIFEDS was developed to improve inertial confinement fusion yields by magnetizing the capsule prior to implosion (*Gotchev et al.*, 2009). According to *Knauer et al.* (2010), "the benefits of this approach are twofold: The hot spot can reach ignition temperatures because of the reduced electron thermal

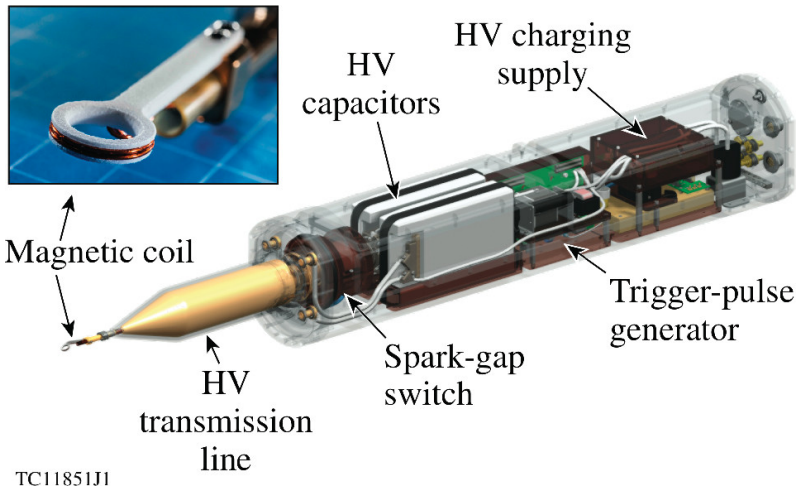

Figure A.1: The Magneto-Inertial Fusion Electrical Discharge System (MIFEDS) is a TIM-based magnetic field generator. (Image credit: *Fiksel et al.* (2015))

conductivity. When the nuclear burn develops, the alpha particles can be confined, by a strong magnetic field, to the burn region delivering the energy where it is needed to support the burn wave." Since being developed for fusion research, it has been used on many experimental platforms, including experiments to study the Weibel instability (*Fox et al.*, 2013) and magnetic recombination (*Fiksel et al.*, 2014).

A.3 Thomson Scattering

Thomson scattering is a method for probing the condition of an experimental plasma by making use of a laser-plasma instability. When a laser beam is incident on an experimental plasma with an underlying density perturbation (and all experimental plasmas have underlying perturbations), wave beating results. In this case, the two waves that beat together are the incident laser wave and the electron density fluctuation wave. This will produce two scattered light waves, one with the sum of the frequencies and wave numbers and one with their differences (*Drake*, 2006).

Because the scattered light waves are driven by the density fluctuation, the scattered spectrum is dependent on on the density and temperature of the plasma. An experimenter may collect the scattered spectrum and compare it to analytically pre-

dicted spectra and thereby determine the plasma conditions that produced it. There will also be an overall Doppler shift to the spectra which indicates the bulk velocity of the plasma.

This section discusses Thomson scattering in depth. Section A.3.1 discusses the conceptual differences between streaked and imaging Thomson scattering, which are both fielded on OMEGA. Section A.3.2 presents the Thomson scattering set-up at OMEGA.

There are two electron density fluctuation waves of interest: the Electron Plasma Wave, or EPW, and the Ion Acoustic Wave, or IAW. The sources of these waves, from which they derive their names, are discussed in Section A.3.4.

To analyze the scattered spectrum, the experimenter compares it to analytically predicted scattered spectra, which are obtained from a numerical code, explained in Section A.3.5. Section A.3.6 presents an example of Thomson data being fit.

Section A.3.7 discusses problems one might encounter in Thomson scattering.

A.3.1 Streaked vs. Imaging Thomson

OMEGA has the ability to field either streaked or imaging Thomson scattering, and the facility is flexible enough to switch from one to the other in the midst of a shot day. Streaked Thomson scattering gathers information about the plasma in a fixed location over an extended period of time. Conceptually, it is similar to installing a flow meter and recording the density, temperature and velocity of the plasma going past it. Imaging Thomson scattering gathers information about a long tube of plasma at a fixed time.

Figure A.2 illustrates the differences in configuration necessary to produce either streaked or imaging Thomson. For streaked Thomson, the probe beam intersects with the experimental plasma, illustrated here as a jet. The volume studied is small, $50\,\mu\text{m} \times 50\,\mu\text{m} \times 50\,\mu\text{m}$. For imaging Thomson, the probe beam illuminates an ex-

tended region, $50\,\mu\text{m} \times 50\,\mu\text{m} \times 1000\,\mu\text{m}$, for a short period of time.

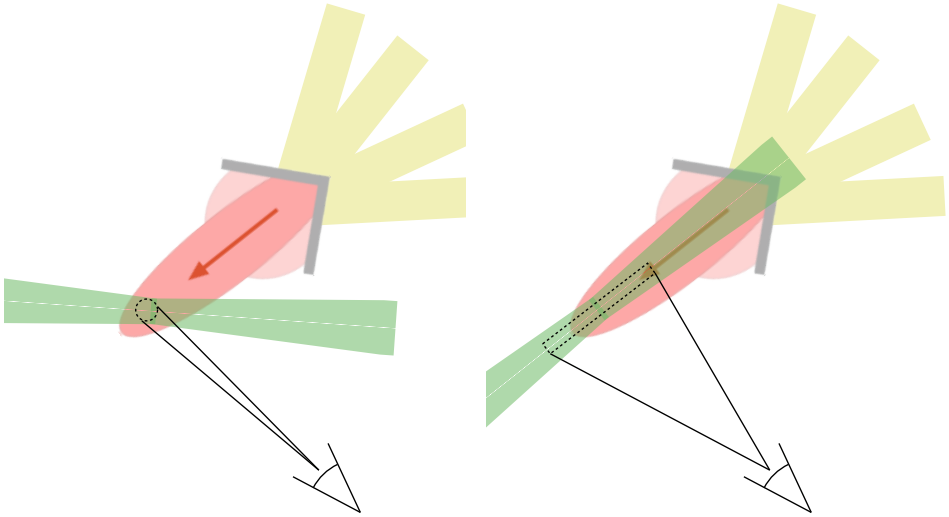

Figure A.2: A comparison of streaked Thomson scattering (left) and imaging Thomson scattering (right). The probe beam (green) illuminates some portion of the jet (pink). (In practice, the drive beams (yellow) would not fire at the same time as the probe.)

A.3.2 OMEGA Thomson Set-up

OMEGA has the ability to field either a 2ω (526.5 nm) or 4ω (263.25 nm) probe beam. The OMEGA probe laser pulse can be anywhere from 100 ps to 3.5 ns long with total energy $10 - 200$ J (*Katz et al.*, 2013).

The system is not permanently installed. On weeks where Thomson is supported, Beam 25 is shifted in frequency and redirected so that it enters the chamber through Port 9. It scatters off experimental plasma at TCC and the scattered light is collected by a telescope TIM 6. Light from the telescope is directed to the Thomson scattering set-up cart about 8 m away, where the beam is broken into a spectrum and recorded. This basic geometry, Port 9 to TCC to TIM 6, cannot be altered; the experimenter must design around it, see Figure A.3.

Once the scattered light is collected and directed to the Thomson scattering set-up, it is split into three legs: one for the EPW feature, one for the IAW feature, and one for

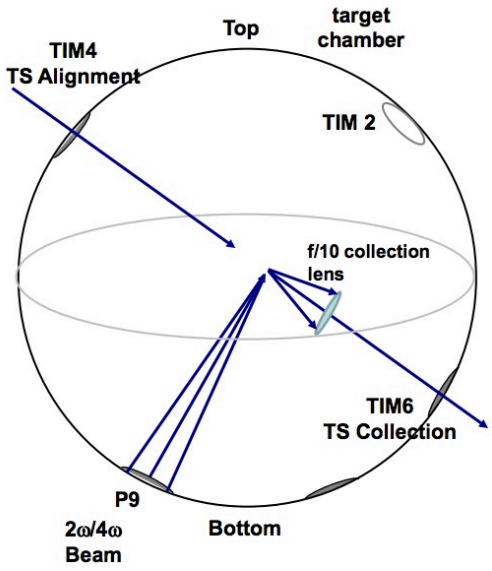

Figure A.3: Schematic for Thomson scattering on OMEGA. The Thomson probe beam enters through Port 9, scatters off experimental plasma at TCC, and is collected through a telescope in TIM 6. (Image credit: Laboratory for Laser Energetics)

the 2-D imager. The first two legs are illustrated in Figure A.4. (See Section A.4 for a discussion of the third leg.) Both the EPW and the IAW legs rely on Czerny-Turner spectrometers, see Figure A.5, which use a grating to split a broadband light beam into a spectrum. The EPW leg uses a 0.3-m (f/5) Czerny-Turner spectrometer; one of three different gratings can be used to obtain a spectral window of 40, 80 or 160 nm. The IAW leg uses a 1-m (f/9) Czerny-Turner spectrometer; its three gratings provide spectral windows of 40, 80 or 160 nm. For both the 0.3-m and the 1-m spectrometers, spectral resolution is about 0.7% of the spectral window (*Katz et al.*, 2012, 2013). When running 2ω scattering, a long-pass filter that blocks wavelengths < 400 nm is used to protect the Thomson set-up from 3ω light (*Katz et al.*, 2013).

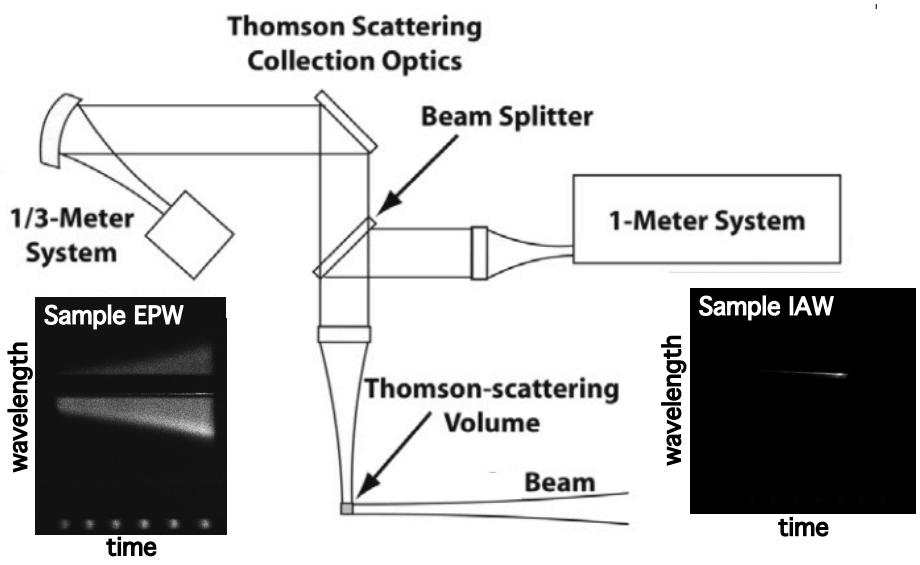

Figure A.4: Beam path diagram for Thomson scattering on OMEGA. The scattered spectrum is split; one leg leads to the EPW 1/3-meter spectrometer and another leads to the IAW 1-m spectrometer. Not shown is the optical path leading to the 2-D optical imager. Optical paths and angles are not to scale. (Image credit: diagram from Laboratory for Laser Energetics; my own data added as examples.)

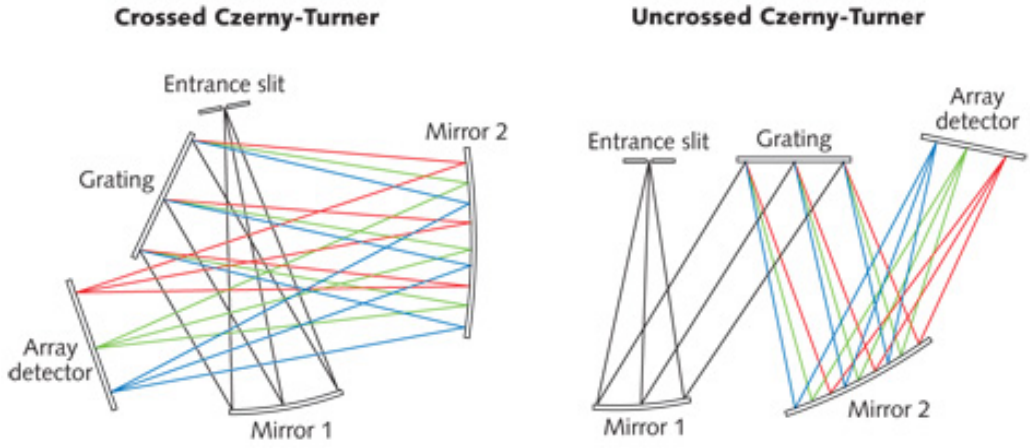

Figure A.5: An unfolded Czerny-Turner spectrograph. A Czerny-Turner spectrograph uses a grating to resolve a spectrum by wavelength. (Image credit: Laser Focus World)

A.3.3 The Electron Plasma and Ion Acoustic Waves

This derivation of the electron plasma wave and ion acoustic wave frequencies follows that of *Bellan* (2006), which begins by assuming an unmagnetized two-fluid plasma.

$$m_\sigma n_{\sigma 0} \frac{d\boldsymbol{u_{\sigma 1}}}{dt} = q_\sigma n_{\sigma 0} \boldsymbol{E_{\sigma 1}} - \nabla P_{\sigma 1} \quad \text{Linearized Eq. of Motion} \tag{A.1a}$$

$$\frac{dn_{\sigma 1}}{dt} + n_0 \boldsymbol{\nabla \cdot u_{\sigma 1}} = 0 \quad \text{Linearized Continuity} \tag{A.1b}$$

$$\boldsymbol{E_1} = -\nabla \phi_1 - \frac{\partial A_1}{\partial t} \quad \text{Linearized Electric Field} \tag{A.1c}$$

$$\frac{P_{\sigma 1}}{P_{\sigma 0}} = \gamma \frac{n_{\sigma 1}}{n_{\sigma 0}} \quad \text{Linearized Eq. of State} \tag{A.1d}$$

Taking the divergence of the linearized equation of motion, substituting both the linearized continuity and the linearized equation of state into it, and making use of the ideal gas law ($P_{\sigma 0} = n_{\sigma 0} \kappa T_{\sigma 0}$, where κ is the Boltzmann constant[1]) yields

$$m_\sigma \frac{\partial^2 n_{\sigma 1}}{\partial t^2} = q_\sigma n_{\sigma 0} \nabla^2 \phi_1 + \gamma \kappa T_{\sigma 0} \nabla^2 . n_{\sigma 1} \tag{A.2}$$

Assuming that both n and ϕ are proportional to $\exp(i\boldsymbol{k} \cdot \boldsymbol{x} - i\omega t)$, means that $\nabla \to i\boldsymbol{k}$ and $\partial/\partial t \to -i\omega$; using these in Equation A.2 yields a purely algebraic form

$$m_\sigma \omega^2 n_{\sigma 1} = q_\sigma n_{\sigma 0} k^2 \phi_1 + \gamma \kappa T_{\sigma 0} k^2 n_{\sigma 1}. \tag{A.3}$$

Poisson's equation relates n and ϕ

$$k^2 \phi_1 = \frac{n_{e1} q_e}{\epsilon_0} + \frac{n_{i1} q_i}{\epsilon_0}. \tag{A.4}$$

[1] Although k is traditional, it is already taken by wave number.

Solving Equation A.3 for $n_{\sigma 1}$ and plugging it into Poisson's equation yields

$$(1 + \chi_e + \chi_i)\phi_1 = 0, \tag{A.5}$$

where χ_σ is known as the susceptibility, defined as

$$\chi_\sigma = -\frac{\omega_{p\sigma}^2}{\omega^2 - \gamma k^2 \kappa T_{\sigma 0}/m_\sigma}, \tag{A.6}$$

and $\omega_{p\sigma}$ is the plasma frequency. For Equation A.5 to be true for all ϕ_1, then

$$1 + \chi_e + \chi_i = 0, \tag{A.7}$$

this is known as the dispersion relation.

There two limiting behaviors of the susceptibility, Equation A.6. If the phase velocity of the density fluctuation, ω/k, is much greater than the thermal velocity, $\sqrt{\kappa T_{\sigma 0}/m_\sigma}$, the behavior is said to be adiabatic. In this scenario, the density fluctuation travels faster than the thermal velocity, so isothermal conditions cannot be maintained and adiabatic conditions exist. On the other hand, if phase velocity of the density fluctuation, ω/k, is much less than the thermal velocity, $\sqrt{\kappa T_{\sigma 0}/m_\sigma}$, the behavior is said to be isothermal. In this scenario, the density fluctuation travels slower than the thermal velocity, so the plasma can maintain a constant temperature. In these cases, the susceptibility reduces as follows

$$\chi_\sigma = -\frac{1}{k^2 \lambda_{D\sigma}^2} \frac{k^2}{\omega^2} \frac{\kappa T_\sigma}{m_\sigma} \left(1 + 3\frac{k^2}{\omega^2}\frac{\kappa T_{\sigma 0}}{m_\sigma}\right) \quad \text{for Adiabatic: } \omega/k \gg \sqrt{\kappa T_{\sigma 0}/m_\sigma}, \text{ and} \tag{A.8a}$$

$$\chi_\sigma = \frac{\sigma_{p\sigma}^2}{k^2 \kappa T_{\sigma 0}/m_\sigma} = \frac{1}{k^2 \lambda_{D\sigma}^2} \quad \text{for Isothermal: } \omega/k \ll \sqrt{\kappa T_{\sigma 0}/m_\sigma}. \tag{A.8b}$$

There are two electron density fluctuations of interest, which are discussed here

qualitatively before being addressed mathematically. For the first scenario, the electron density fluctuation is assumed to travel much faster than either the electron or the ion thermal velocity and both the electron and ion behavior are treated adiabatically. Because electrons are so much lower in mass, their behavior dominates and the ion behavior can be neglected in this case entirely. Physically, in this case where the ions are stationary and the electrons oscillate. This is the Electron Plasma Wave, or EPW.

For the second scenario, the density fluctuation velocity is assumed be between the electron and ion thermal velocity; that is, greater than the ion thermal velocity and less than the electron thermal velocity. Therefore the ions are treated adiabatically and the electrons are treated isothermally. Physically, this is the case where the ions oscillate and thereby force the electrons to oscillate as well. (Because of the difference in mass, ions can ignore electrons, but not vice versa.) This is the Ion Acoustic Wave, or IAW.

To address the EPW, both electrons and ions are taken to be adiabatic. After substituting Equation A.8a into Equation A.7, dropping the ion contribution because $\omega_{pe}^2 \gg \omega_{pi}^2$, and using the zeroth order solution, $\omega = \omega_{pe}$, in the thermal term, the expression for the electron plasma wave frequency becomes

$$\omega^2 = \omega_{pe}^2 + 3k^2 \frac{\kappa T_{e0}}{m_e}. \tag{A.9}$$

To address the IAW, the ions are taken to be adiabatic and the electrons are taken to be isothermal. Substituting Equation eq:suscept-iso for the electron contribution and Equation eq:suscept-ad for the ion contribution to the dispersion relation, defining an ion acoustic velocity, $c_s^2 = kT_e/m_i$, and once again using the zeroth order solution

in the thermal term yields the expression for the ion acoustic wave frequency,

$$\omega^2 = \frac{k^2 c_s^2}{1 + k^2 \lambda_{De}^2} + 3k^2 \frac{\kappa T_{i0}}{m_i}. \tag{A.10}$$

A.3.4 Predicting EPW and IAW Peaks

As seen in Figure A.6, an incident wave with k-vector $\mathbf{k}_i$ scatters off a moving charge to create $\mathbf{k}_s$, $\mathbf{k} = \mathbf{k}_s - \mathbf{k}_i$; there is an angle θ between the two k-vectors. For Thomson scattering, there will be an overall Doppler shift depending on $\mathbf{kv}$ where $\mathbf{v}$ is the bulk velocity of the plasma. Ideally, the experiment is designed such that $\mathbf{k}$ and $\mathbf{v}$ are parallel. The $\mathbf{k}$, therefore, is also fixed and the experiment is typically designed around it.

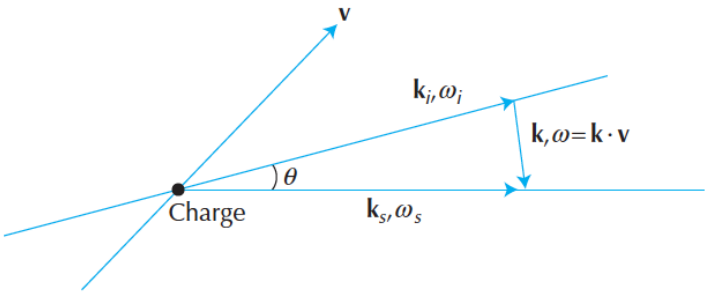

Figure A.6: Scattering k-vector diagram. (Image credit *Froula et al.* (2011))

This derivation follows *Froula et al.* (2011). The incident and scattered waves are governed by the dispersion relations,

$$k_i^2 c^2 - \omega_i^2 + \omega_{pe}^2 = 0, \tag{A.11a}$$

$$k_s^2 c^2 - \omega_s^2 + \omega_{pe}^2 = 0, \tag{A.11b}$$

where k is the wavenumber, c is the speed of light, ω is the frequency, and ω_{pe} is the electron plasma frequency.

From the law of cosines, we see that $|k| = (k_s^2 + k_i^2 - 2k_s k_i \cos\theta)^{1/2}$. For $v/c \ll 1$, the difference between k_s and k_i is small (small Doppler shift), and this reduces to

$$|k| \simeq 2|k_i| \sin(\theta/2). \tag{A.12}$$

A.3.4.1 Ion Acoustic Wave

The spectrum will have an overall Doppler shift according to

$$\frac{\Delta\lambda}{\lambda_i} = \sqrt{\frac{1 - v/c}{1 + v/c}} - 1, \tag{A.13}$$

where v is the velocity parallel to $\mathbf{k}$ and c is the speed of light. For an incident wave of $\lambda_i = 526.5$, the Doppler shift will range from about 0.1 nm for a plasma flowing at $50\,\mathrm{km\,s^{-1}}$ to a shift of 1 nm for a plasma flowing at $500\,\mathrm{km\,s^{-1}}$. Although technically, the Doppler shift affects both the IAW and EPW portions of the spectra, in practice the shifts are too small to be visible in the EPW spectra.

The ion acoustic dispersion relation from *Froula et al.* (2011) (Eq. 5.3.9) is,

$$\omega_{iaw} \simeq \pm k \left(\frac{\alpha^2 Z \kappa T_e}{(1 + \alpha^2) m_i} + \frac{3\kappa T_i}{m_i} \right)^{1/2}, \tag{A.14}$$

where ω_{iaw} is the IAW frequency, $\alpha = 1/k\lambda_{De}$ where λ_{De} is the Debye length, Z is the ionization, and κ is the Boltzmann constant; this is simply a rearrangement of Equation A.14. The frequency separation between the peaks will be twice this. Substituting the expression for k, $k_{iaw} \simeq 2k_i \sin(\theta/2)$ (Eq. A.12), into Equation A.14 results in

$$\Delta\omega_{iaw} \simeq 4k_i \sin\left(\frac{\theta}{2}\right) \left(\frac{Z \kappa T_e}{(1 + k_{ia}^2 \lambda_{De}^2) m_i} + \frac{3\kappa T_i}{m_i} \right)^{1/2}, \tag{A.15}$$

This is expression is easier to use when written in terms of wavelength. Because

$\Delta\lambda/\lambda = \Delta\omega/\omega$, and $k = \omega/c$,

$$\frac{\Delta\lambda_{iaw}}{\lambda_i} \simeq \frac{4}{c}\sin\left(\frac{\theta}{2}\right)\sqrt{\frac{\kappa T_e}{m_i}\left[\frac{Z}{(1+k_{iaw}^2\lambda_{De}^2)}+\frac{3T_i}{T_e}\right]}. \tag{A.16}$$

which is Eq. 5.4.4 from *Froula et al.* (2011).

As seen from Equation A.16, the separation between the IAW peaks depends on T_e and T_i, not n_e, and as seen in Figure A.7 the separation varies from roughly 0.1 to 1 nm in the range of temperatures of interest. As noted above, this is on the same scale as the Doppler shift.

A.3.4.2 Electron Plasma Wave

Beginning with the electron plasma wave dispersion relation, Equation A.9, and substituting Eq. A.11a and A.11b, and assuming that,

$$\frac{\omega_{pe}^2}{c^2k_i^2} = \frac{4\pi n_e e^2}{m_e c^2 k_i^2} = \frac{n_e}{n_c}, \tag{A.17}$$

where n_c is the critical electron density (see Section A.3.7), yields the separation expression for EPW waves, Eq. 5.4.6 in *Froula et al.* (2011):

$$\frac{\Delta\lambda_{epw}}{\lambda_i} \simeq 2\left[\frac{n_e}{n_c}+\frac{3\kappa T_e}{m_e c^2}\right]^{1/2}\left(1+\frac{3}{2}\frac{n_e}{n_c}\right). \tag{A.18}$$

As seen from Equation A.18, the separation between the EPW peaks depends increases with increasing n_e and T_e, and as seen in Figure A.7, in the range of plasma parameters we care about ranges from 20 to 200 nm. Earlier we stated that $0.1n_c$ was a rule of thumb limit for Thomson scattering. As seen from Figure A.7, as the electron density approaches this limit, the n_e/n_c term dominates and the separation does not change much with T_e. This is another indication that Thomson scattering is becoming less useful as the limit is approached.

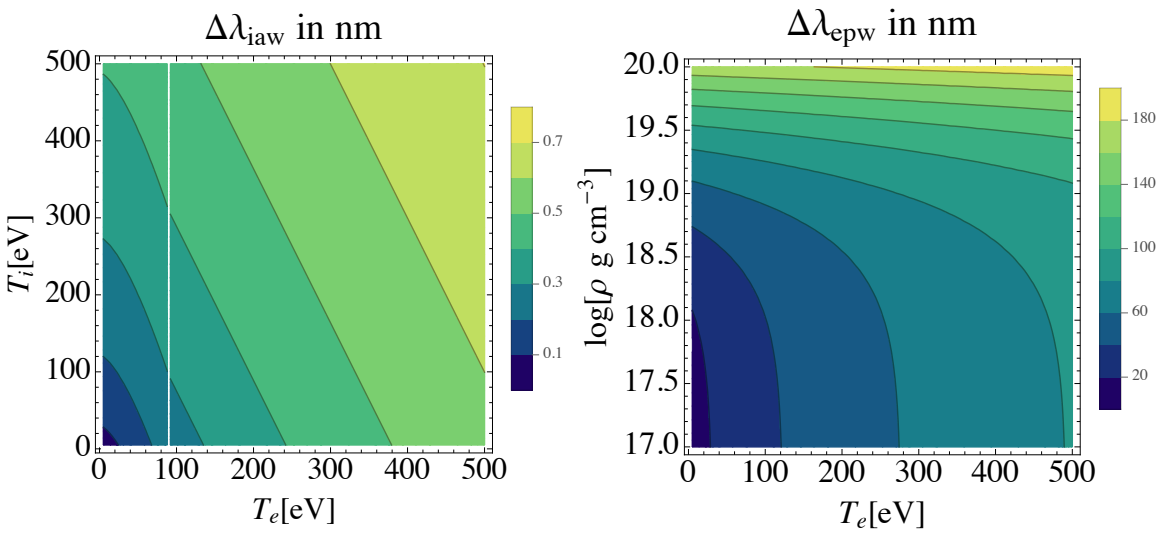

Figure A.7: Typical IAW and EPW peak differences. $\Delta\lambda_{iaw}$ (left) and $\Delta\lambda_{epw}$ (right) for typical ranges of experimental plasma parameters.

A.3.5 Numerically Calculating the Form Factor

A.3.5.1 Formulae

The form factor, Eq. D.1 in *Froula et al.* (2011), is

$$S(k,\omega) = \left|\frac{1+\chi_i}{\epsilon}\right|^2 f_e(\omega/k) + Z\left|\frac{\chi_e}{\epsilon}\right|^2 f_i(\omega/k), \tag{A.19}$$

where k is the wave number, ω is the frequency, $f_e(\omega/k)$ and $f_e(\omega/k)$ are the normalized, one-dimensional electron, and χ_e and χ_i are the electron and ion contributions to the dielectric function, $\epsilon = \chi_e + \chi_i + 1$.

The velocity distributions, $f_e(\omega/k)$ and $f_i(\omega/k)$, are

$$f_\alpha(\omega/k) = \left(\frac{1}{2\pi}\right)^{1/2}\left(\frac{c}{v_{th,\alpha}}\right) e^{-\omega^2/(2k^2 v_{th,\alpha}^2)}, \tag{A.20}$$

where α may either be e or i, and $v_{th,\alpha}$ is the thermal velocity.

The dielectric function components, χ_e and χ_i, are

$$\chi_\alpha(\omega, k) = -\frac{1}{2}\frac{1}{(k\lambda_{d,\alpha})^2}\frac{\delta}{\delta\xi}W(\xi), \tag{A.21}$$

where $\lambda_{d,\alpha}$ is the Debye length and W is the plasma dispersion function, expressed as a function of the parameter $\xi = \omega/\sqrt{2}kv_{th,\alpha}$,

$$W(\xi) = \left(\frac{1}{\pi}\right)^{1/2}\int_{-\infty}^{\infty} dz\frac{e^{-z^2}}{z-\xi}. \tag{A.22}$$

A.3.5.2 Numerical Code

Thomson spectrum calculator takes the following inputs:

- The electron temperature, T_e, in eV.
- The ion temperature, T_i, in eV.
- A vector with the *maximum* ionization state, Z, for each species in the plasma. For CH plasma, $Z = [1, 6]$.
- A vector with the atomic weight (in proton masses), A, for each species in the plasma. For CH plasma, $A = [1, 12]$.
- A vector with the fractional composition of each species in the plasma. For CH plasma, fract $= [0.5, 0.5]$.
- The electron number density, n_e, in cm^{-3}.
- The velocity parallel to the k-vector, v_a, in $\mathrm{cm\,s}^{-1}$.
- The drift velocity of the electrons relative to the ions, u_d, in $\mathrm{cm\,s}^{-1}$.
- The scattered frequency, ω_s, in $\mathrm{rad\,s}^{-1}$. ω_s is an array with several thousand values centered on ω_L, the frequency of the incident laser probe beam. The

purpose of the code is to obtain a vector S, the scattered power spectrum, as a functions of ω_s.

- The frequency of the incident laser probe beam, ω_L, in $\mathrm{rad\,s^{-1}}$.
- The scattering angle, θ, in degrees. (The code calls this "sa".) For the set-up at OMEGA, $\theta = 63°$.
- The angle between the plane of polarization and the scattering plane, ϕ, in degrees. For the set-up at OMEGA, $\phi = 90°$.
- The angle in degrees, γ, between the drift velocity, u_d, and the k-vector. For the set-up at OMEGA, $\gamma = 0°$.

The code published in *Froula et al.* (2011) takes the following steps:

1. Before running the Thomson predictor, run a separate code to create a table $\xi \rightarrow (k\lambda_{d,\alpha})^2\chi_\alpha$.
2. The code takes in ω_L, the frequency of the incident laser, and ω_s, an array of scattered frequencies centered on ω_L, as inputs. It finds $\omega = \omega_s - \omega_L$, where ω, like ω_s is an array.
3. Find k_s by solving $\omega_s^2 = \omega_{pe}^2 + c^2k_s^2$. k_s is also an array.
4. Find k using the Law of Cosines and the scattering angle $k^2 = k_s^2 + k_i^2 - 2k_sk_i\cos\theta$. At this point, the code has four arrays: ω_s, the range of scattered frequencies for which we want to find $S(k,\omega)$, and arrays with the corresponding values of ω, k_s, k.
5. Calculate the various plasma quantities such as v_{th} and λ_D.
6. For every value in the array ω_s,
   (a) Get the corresponding values of ω and k.

(b) Calculate ξ.

(c) Use the $\xi \rightarrow (k\lambda_{d,\alpha})^2\chi_\alpha$ table to find $(k\lambda_{d,\alpha})^2\chi_\alpha$.

(d) Plug everything into Equation A.19 to find $S(k,\omega)$.

7. Convert ω_s to λ_s. Normalize the scattered spectrum and plot it against λ_s.

A.3.6 Example of Spectra Fitting

Every experimental spectrum is hand fit using the spectrum generator discussed in Section A.3.5. The plasma parameters (n_e, T_e, T_i, and v_a) are varied and the predicted spectrum is plotted alongside the experimental data until a close fit is obtained, see Figures A.8 and A.9, which show a pair of spectra obtained in April 2012.

The electron plasma wave spectrum is used to determine n_e and T_e, while the ion acoustic wave spectrum is used to determine v_a and T_i. As seen in Figure A.9, the IAW spectra from April 2012 were not clear enough to distinguish between different values of T_i.

A.3.7 Problems Encountered in Thomson Scattering

In addition to the geometry concerns discussed in Section A.3.2, there are four additional concerns to consider:

1. The density is too low and the plasma is not in the collection scattering regime.

2. The density is too high and the probe beam reflects off the plasma.

3. The probe energy is too high and heats the experimental plasma significantly.

A.3.7.1 Collective vs. Non-Collective

At what density does a plasma scatter incident radiation collectively? Consider two scale lengths: the wavelength of incident wave and the Debye wavelength, "the

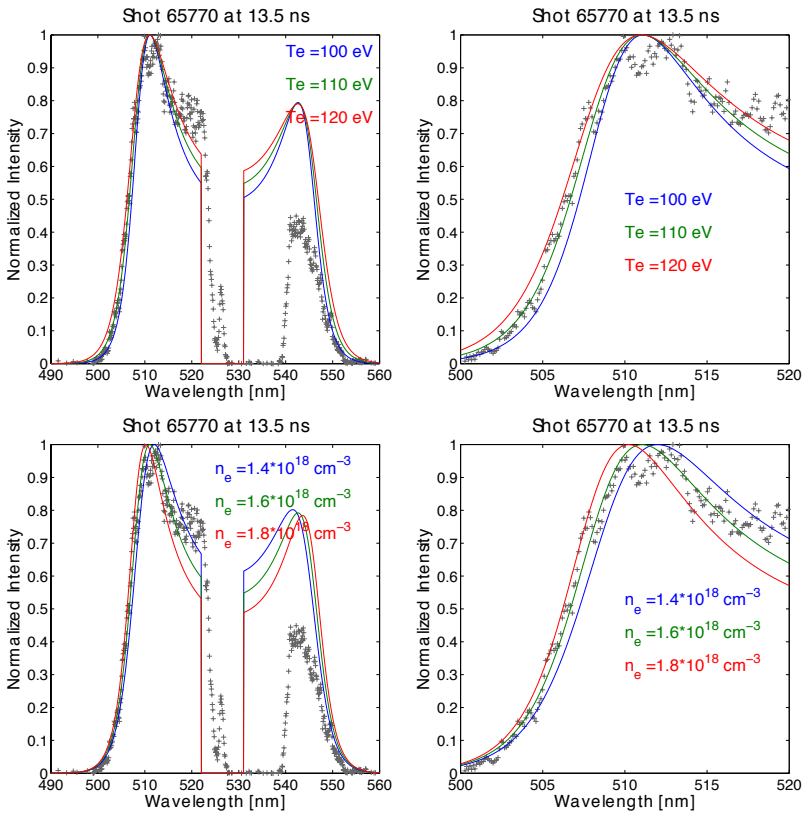

Figure A.8: An example of fitting EPW data. Fitting single jet spectrum taken 13.5 ns after drive. Above: the full spectrum with three potential T_e values (left) and zoomed view of the higher peak (right). Below: the full spectrum with three potential n_e values (left) and zoomed view of the higher peak (right). This spectrum (taken 13.5 ns after drive) had the best fit with $T_e = 110\,\text{eV}$ and $n_e = 1.6 \times 10^{18}$.

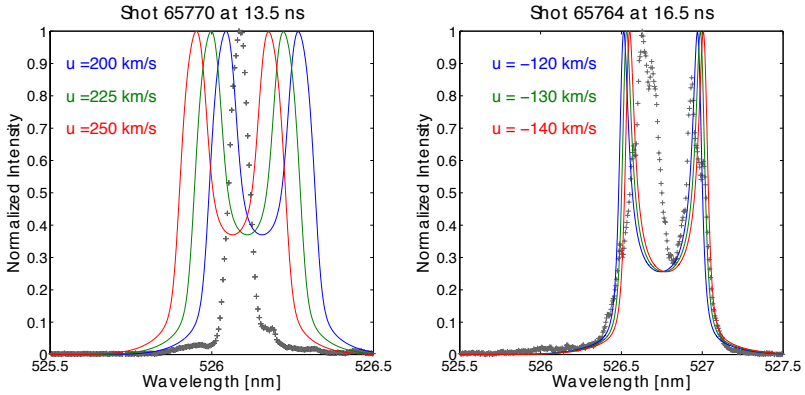

Figure A.9: An example of fitting IAW data. Many IAW appeared to have erroneous peaks of reflected light, but velocity data could still be obtained by fitting the Doppler shift. Left: the IAW data corresponding to Figure A.8. Right: One of the clearest examples of a IAW data we obtained.

characteristic distance over which the potential of a charge is shielded by neighboring charges" (*Froula et al.*, 2011).

If the Debye wavelength is smaller than the wavelength of the incident wave, the wave "sees" many charges together and the scattering will be collective. If the wavelength of the incident wave is smaller than the Debye wavelength, the wave "sees" the charges individually and the scattering will be non-collective.

If we introduce a parameter α,

$$\alpha = \frac{1}{k\lambda_{De}} = \frac{1.08 \times 10^{-4}\lambda_i \,\mathrm{cm}}{\sin\theta/2}\left[\frac{n_e \,\mathrm{cm}^{-3}}{T_e \,\mathrm{eV}}\right]^{1/2}, \tag{A.23}$$

then $\alpha \ll 1$ is non-collective and $\alpha \gg 1$ is collective. Here we have once again made use of $k \simeq 2k_i \sin(\theta/2)$.

Figure A.10 shows α over a range of typical experimental parameters for a 2ω (526.5 nm), $\theta = 63°$ Thomson scattering set-up. For low temperatures ($T_e < 20\,\mathrm{eV}$), collective ($\alpha > 1$) scattering occurs at electron densities above $10^{17}\,\mathrm{g\,cm^{-3}}$. At higher temperatures, the electron density must be somewhat higher ($> 10^{18}$) for collective scattering.

A.3.7.2 Critical Density

At what point does the plasma become too dense for the incident wave to penetrate it? Referring to A.11a,

$$k_i^2 c^2 - \omega_i^2 + \omega_{pe}^2 = 0 \tag{A.24}$$

for $\omega_i > \omega_{pe}$, the wavenumber k_i is real and the wave is transmitted through the plasma; for $\omega_i < \omega_{pe}$ the wavenumber is imaginary and the wave is not transmitted. The electron density at which $\omega_{pe} = \omega_i$ is the critical density,

$$n_c = \frac{\omega_i^2 m_e}{4\pi e^2} = \frac{\pi c^2 m_e}{\lambda_i^2 e^2}. \tag{A.25}$$

As an example, for 526.5 nm, $n_c = 4 \times 10^{21}$ cm^{-3}. As a rule of thumb, densities below $0.1n_c$ are considered reasonable to attempt with Thomson scattering.

A.3.7.3 Probe Heating

As the probe beam scatters off the experimental plasma, some fraction of it is absorbed and heats the plasma. At what point does this become significant enough to interfere with Thomson scattering? The maximum temperature increase can be estimated by comparing the energy deposited per unit volume to the thermal energy per unit volume. For example, if the energy deposited is equal to the initial thermal energy then we might expect the temperature to double, at most.

Average power dissipated (in MKS, eq. 6.6.3 from *Froula et al.* (2011))

$$W_D = \frac{n_e e^2 \nu_{ei}}{m_e c \epsilon_o \omega_i^2} \frac{P_i}{A} \tag{A.26}$$

Dividing this by the $\frac{3}{2}\kappa T_e n_e$, yields the estimated fractional temperature increase, Eq. 6.6.6 in *Froula et al.* (2011)

$$\frac{\Delta T_e}{T_e} \simeq 1.28 \times 10^5 \frac{n_i \ln \Lambda}{\omega_i^2 A [T_e]^{5/2}} \int_0^\tau P_i dt, \tag{A.27}$$

where $\ln \Lambda$ is Coulomb lambda, A is the mean ion mass in m_p, and $\int_0^\tau P_i dt$ is the incident power integrated over the pulse length. All quantities in Eq. A.27 are in CGS units except T_e, which is in eV. As seen in Figure A.10, probe heating will exceed 10% for most experimental plasma conditions.

A.4 Visible Light Imaging

As related in Section A.3.2, when the Thomson scattering set-up is installed, a telescope in TIM 6 collects light from TCC and directs it the Thomson cart, where it

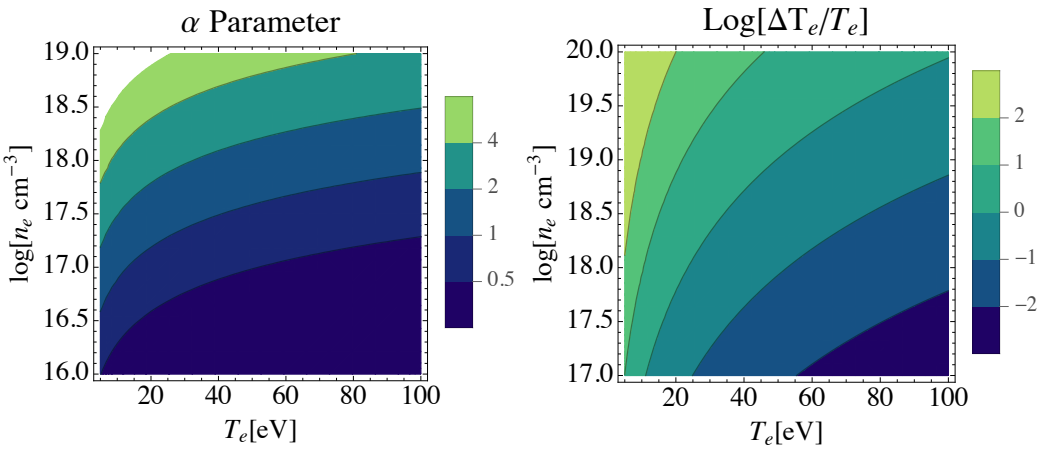

Figure A.10: Problems typically encountered in Thomson scattering. Left: $\alpha = 1/(k\lambda_{De})$ calculated for a 2ω Thomson set-up at OMEGA. Right: Probe heating calculated for a 20 J, 2ω Thomson set-up at OMEGA.

is spilt into three legs: one for EPW, one for IAW, and one for the 2-D imager. This 2D imager is known as the Two Plasmon Decay Imager, or TPDI. The 2-D imager was originally added to the cart as ride-along diagnostic, something that could provide a bit of extra data and that could help to troubleshoot problems with Thomson scattering. However, it has since become the most reliable 2-D visible light imager at OMEGA.

In layman's terms, TPDI simply takes a picture of TCC. Its field of view depends on which telescope is installed; the experimenter can request either a 2 mm or 4 mm field of view. TPDI is typically filtered with a long-pass filter to protect it from 3ω light and one or several neutral density filters.

TPDI has a minimum gate length of 3 ns. Timing of TPDI does not need to be coincident with the drive beams or the probe beam. Nor does the rest of the Thomson set-up need to be used with TPDI; for this thesis project, TPDI was used alone for the accretion shock experiment.

APPENDIX B

Summary of Shot Days

This appendix provides a detailed summary of the shot days themselves. The motivations of the experiments, the data collected, and the analysis of that data were addressed in Chapters III, IV, and V. This appendix includes information that would be of interest to a fellow OMEGA user: the TIM assignments, shot sequences, and so forth. The shot days are as follows:

1. April 2012—A full shot day devoted to testing a new method of creating collimated plasma jets. Jets were fired individually and in head-on collisions and were probed with 2ω Thomson scattering. Both the jet-creation method and 2ω Thomson scattering proved successful and both were used on subsequent shot days. See Section B.1. Complete data for this day are in Appendix C.

2. August 2013—A full shot day devoted to the idea of creating a scaled accretion disk inside an imposed cusp magnetic field. Difficulties encountered during this shot day, along with questions about the inherent feasibility of scaling an entire accretion disk in a laboratory experiment, lead to the scope of the project narrowing. Section B.2. Complete data for this day are in Appendix D.

3. May 2014—The first shot day devoted to pursuing the idea of creating a scaled accretion shock in the laboratory. Half the day was devoted to the accretion shock experiment, half was devoted to continued probing of plasma jets with Thomson scattering. Unfortunately, the primary diagnostic on this shot day, proton radiography, failed. See Section B.3. Complete data for this day are in Appendix E.

4. May 2015—A second full shot day devoted to improving on the design of the May 2014 experiments. The targets were redesigned to allow proton both radiography and visible light imaging along opposite (180° apart) lines of sight. Unfortunately, proton radiography failed once again, albeit for a different reason than in May 2014. Visible light imaging was successful. See Section B.4. Complete data for this day are in Appendix F.

5. October 2015—Visible light imaging failed for one shot in May 2014. To fill in this data gap, we used two shots from a shot day devoted to a different campaign to retake the data. These shots have been included in Section B.4 as well. Complete data for this day are in Appendix F.

B.1 April 2012

B.1.1 Collaboration

I served as the graduate student primary investigator for this shot day under the guidance of Carolyn Kuranz and R. Paul Drake (both University of Michigan). The lead engineer for target manufacturing was Sallee Klein (Michigan) and CRASH simulations to help time the shots were performed by Ryan Sweeney (Michigan). Christine Krauland, then a senior graduate student at Michigan, was not deeply involved in the science of the shot day, but accompanied us to OMEGA and acted as a graduate student mentor for my first shot day.

The primary diagnostic for this shot day was Thomson scattering, and two Lawrence Livermore National Laboratory (LLNL) scientists joined the collaboration as experts in Thomson scattering: Dustin Froula (who has since moved to LLE) and Steve Ross.

B.1.2 Configuration

As discussed in Chapter III, the purpose of the April 2012 shot day was to test a method for creating collimated plasma jets. We launched jets through rear irradiation singly and in head-on collisions. Table B.1 lists the experimental parameters for April 18, 2012.

B.1.3 Shot Sequence

As noted in Table B.1, the two experimental targets were positioned using the dedicated target positioner in H2 and a TIM-based target positioner in TIM 4. We began shooting the H2 target alone. On shot days that use Thomson scattering as a diagnostic, TIM 4 (which sits opposite to TIM 6, the Thomson scattering TIM) is reserved for aligning the Thomson scattering set-up. Once Thomson scattering is aligned and several shots have used it successfully, the facility feels comfortable removing the alignment cart and using the TIM for something else. The first four shots of the day, 65762-65, were H2-only shots at various timings. We found that firing the Thomson probe 7 ns after drive was too early, but good data was obtained at 12 ns and 15 ns.

The facility was satisfied that alignment was complete and we were able to switch to using TIM 4 for target positioning. We shot the TIM 4 target alone at 15 ns, Shot 65766, for comparison with the 15-ns H2-only shots, then moved on to shooting both targets at once. We shot head-on collision shots at 15 ns and 20 ns, Shots 65767 and 65769; Shot 65769 was too late and the probe beam reflected off the plasma instead of penetrating and scattering. Finally, we filled out our data with two shots at 12 ns,

Shot 65770, a TIM 4-only shot, and 65774, a collision shot.

Table B.3 contains a list of shots and Table B.3 lists whether data was successfully taken for each one. This was a very successful day; losing a few shots due to probing too early or late is not only expected but desirable: it sets boundaries for where good data can be obtained. All told, we were able to use Thomson scattering to measure electron density, electron temperature and velocity from 12 ns to 18 ns, and we obtained multiple clear images of single and colliding jets evolving with time. Appendix C contains the complete data for this shot day and Chapter III provides discussion of the data.

B.1.4 Difficulties Encountered

We were remarkably fortunate and few difficulties were encountered. We found that the Gated Optical Imager produced poor images, while the imager attached to the Thomson scattering set-up (TPDI) produced high-quality images, see Figure B.1. Resultantly, we chose to never use GOI again.

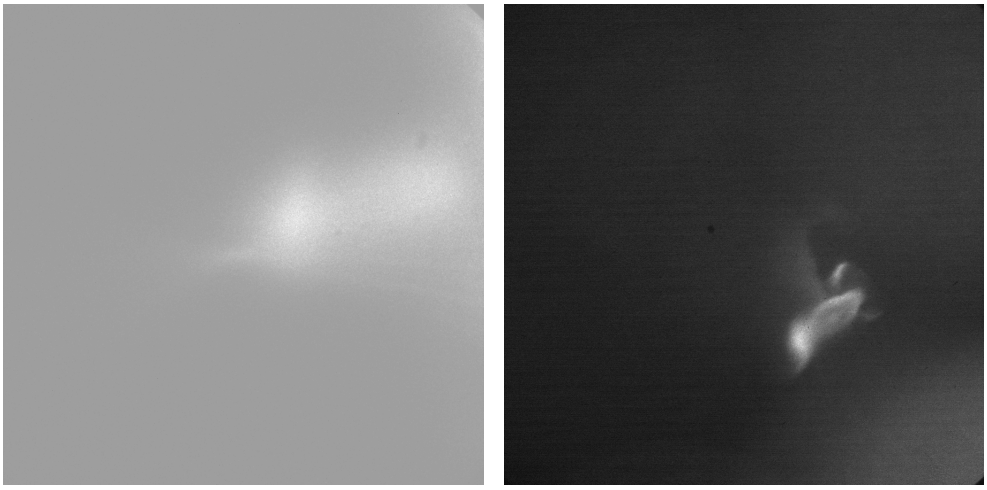

Figure B.1: A comparison of GOI (left) and TPDI (right) for shot 65766. The images are not expected to be identical, as the lines of sight and timings are different, but it is immediately obvious that one is either blur or lens flare, while the other is a recognizable jet.

Target	
Material	CH
Solid density	$1.18\,\mathrm{g\,cm^{-3}}$
Cone opening angle	160°
Cone diameter	2 mm
Cone thickness	$100\,\mu$m
Distance to TCC	3 mm
Drive Beams	
Drive beam wavelength	351 nm (3ω)
Number beams	7 per cone
Total drive energy	3150 J
Drive beam shape	1 ns, square
Drive beam radius	$352\,\mu$m (SG4)
Drive irradiance	$8 \times 10^{14}\,\mathrm{W\,cm^{-2}}$
2ω Thomson beam	
Wavelength	526.5 nm
Energy	120 J
Shape	3 ns, square
Radius	$70\,\mu$m (best focus)
Angle between probe and collector	116.8°
TIM assignments	
TIM 1	Gated Optical Imager
TIM 2	Empty
TIM 3	Empty
TIM 4	TSS alignment or Target positioner
TIM 5	Off-axis ASBO telescope
TIM 6	Thomson scattering set-up (TSS)
H2	Target positioner (Thom. exp.)

Table B.1: Experimental parameters for April 2012. (Note: TIMs 2 and 3 were devoted to the other campaign, which utilized two shots out of this shot day.)

Shot Number	SRF	Cone(s) Driven	Driver Timing	Thomson Timing	TPDI Timing	Thomson Energy
65762	38542	H2	−7 ns	0 ns	10 ns	120 J
65763	39305	H2	−12 ns	0 ns	10 ns	120 J
65764	39306	H2	−15 ns	0 ns	10 ns	120 J
65765	39389	H2	−15 ns	0 ns	10 ns	120 J
65766	38543	TIM 4	−15 ns	0 ns	10 ns	120 J
65767	38493	Both	−15 ns	0 ns	10 ns	120 J
65769	39302	Both	−20 ns	0 ns	10 ns	120 J
65770	39307	TIM 4	−12 ns	0 ns	8 ns	120 J
65774	39303	Both	−12 ns	0 ns	8 ns	120 J

Table B.2: Shots on April 18, 2012. TPDI filtering was ND 1.0 plus long pass filter for all shots. (Note: two shots on this day (65772 and 65773) were devoted to another campaign and are not included here.)

Shot Number	SRF	EPW Data?	IAW Data?	TPDI Data?	Notes
65762	38542	✗	✗	✗	Too early
65763	39305	✓	✓	✗	Target blocked view (see note)
65764	39306	✓	✓	✗	Target blocked view (see note)
65765	39389	✓	✓	✗	Target blocked view (see note)
65766	38543	✓	✓	✓	Good single jet image
65767	38493	✓	✓	✓	Good colliding jet image
65769	39302	✗	✗	✓	Density too high; probe reflected
65770	39307	✓	✓	✓	Good single jet image
65774	39303	✓	✓	✓	Best colliding jet image

Table B.3: Data taken on April 18, 2012. Note: For single jet experiments with the target mounted in H2, the target itself blocks the view of the jet. These images are clear, but there is little to see.

B.2 August 2013

B.2.1 Collaboration

The collaboration for this shot day was built off of that of April 2012. Once again, I was the graduate student primary investigator, working under Carolyn Kuranz and R. Paul Drake. The target manufacturing was lead by Sallee Klein and CRASH simulations were performed in support of the project by Matthew Trantham and Michael Grosskopf. The Thomson scattering collaboration from April 2012 also carried over; both Dustin Froula and Steve Ross were involved.

As this shot day added two additional systems at OMEGA, we expanded our collaboration. Gennady Fiksel was the lead scientist at OMEGA for MIFEDS, with Po-Yu Chang (an OMEGA post-doc) and graduate student Daniel Barnak (University of Rochester) working underneath him. Chikang Li (Massachusetts Institute of Technology) joined the collaboration to lead proton radiography, with then-graduate student Alex Zylstra working with him.

B.2.2 Configuration

As discussed in Chapter V, the August 2013 shot day was intended to serve as a stepping stone towards creating a rotating plasma disk with a "twisted wagon wheel" design.

We built two configurations for August 2013, both intended to work towards the *Ryutov* (2011) disk scheme. As seen in Table B.4, both configurations were designed to launch three jets, alone or in a colliding experiment. Table B.5 lists all the vital statistics for the experiment.

For imaging Thomson, the probe beam must illuminate an extended (in space) section of the experiment, which means the experimenter has fewer choices about how to position the experiment relative to the fixed Thomson probe beam. Generally,

	Imaging Thom. Config.	MIFEDS Config.
Primary purpose	Imaging Thomson	Colliding jets
Launch mechanism	Rear irrad., 4 beams	Rear irrad., 4 beams
Number jets	3	3
Magnetic field?	No	Yes, MIFEDS
Thomson scattering?	Imaging	Streaked
Proton radiography?	No	Yes
Targets in chamber	1 (exp.)	2 (exp.+MIFEDS, BL)

Table B.4: Similarities and differences for the two configurations of August 2013

experimenters choose to align the probe with the flow direction of the experiment; we chose to align the probe beam with Jet B, the central jet. Because the probe beam was aligned with Jet B, imaging Thomson could only be used with this Jet. It was, however, possible to use streaked Thomson with any of the three jets, since for streaked Thomson to work the jet and the beam only have to overlap at TCC.

The Imaging Thomson Configuration described in Table B.4 used a semi-circular target with three cones; a CAD (VisRad) rendering of this target from two different angles can be seen in Figure B.2. Whereas the April 2012 targets were machined out of solid CH, these targets were 3-D printed, except for the cones, which were attached later with glue.

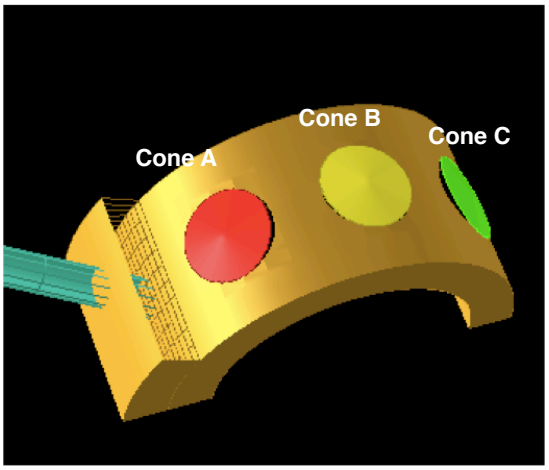

Figure B.2: The imaging Thomson target of August 2013. Three jets can be launched, together or individually, and the imaging Thomson probe is aligned with the central jet, B.

The MIFEDS Configuration described in Table B.4 also had the capability to launch as many as three plasma jets and was designed around magnetic field generation and proton radiography. Like the Imaging Thomson Configuration, it consisted of three cones each 45° apart, which lay in the midplane of a cusp field, with a proton-generating backlighter 1 cm below the experiment and CR-39 30 cm above the experiment.

To build the target for this configuration, the entire support apparatus (the support for the MIFEDS wires, the semi-circular cone base and the stalk/support arm mounting it in TIM 1) was 3-D printed as one piece, then the cones were glued on and wire for the MIFEDS coils was wrapped around it. This (3-D printing followed by wire wrapping) is the normal way to make MIFEDS coils, but building the experimental target into the MIFEDS coil was something that had not been tried before, see Section B.2.4.2. This configuration also called for a proton backlighter, which was mounted in TIM 3.

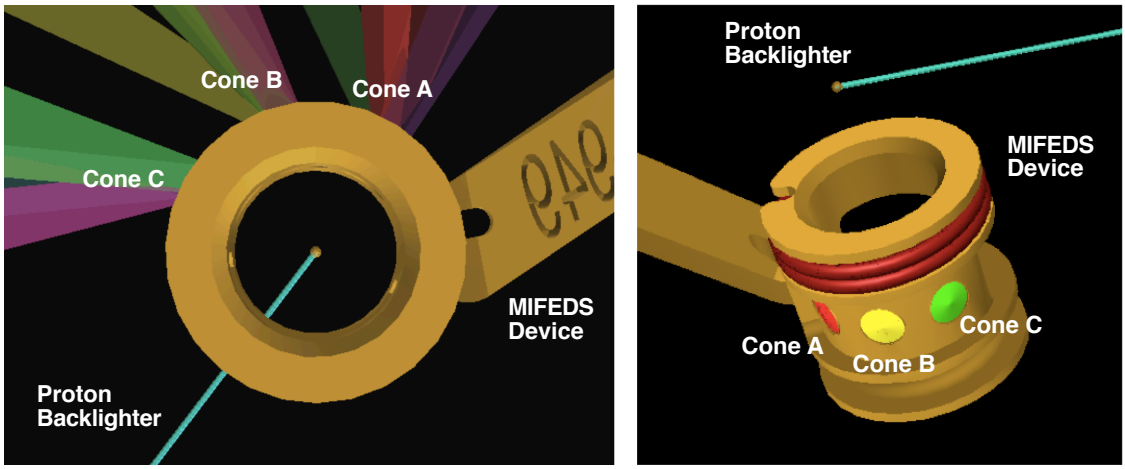

Figure B.3: CAD renderings of the MIFEDS Configuration of August 2013. In the left image, the laser beams have been included; in the right they have been omitted.

B.2.3 Shot Sequence

Table B.6 lists the shots from August 15, 2013 and Table B.7 indicates whether data was obtained. Proton radiography data is not available until weeks later, so the only feedback we had on shot day was Thomson scattering.

We began the shot day with the MIFEDS Configuration. The Thomson probe beam in on the same leg as the proton backlighter beams, and all beams on a given leg must use the same pulse shape. Therefore because the backlighter needed a 1-ns pulse, the streaked Thomson scattering was required to use one as well. We shot Jet B only, first with drive beams 18 ns before the Thomson probe (Shot 70672) and then with drive 25 ns before (Shot 70673). Neither of these shots produced good Thomson data.

We decided to switch to Jet C and go later still, to 30 ns (Shot 70674). This shot produced good Thomson data, both EPW and IAW. At that point we decided to try to obtain imaging Thomson data. To pinpoint the timing we would need, we began shooting the Imaging Thomson Configuration with a long probe pulse, 3 ns. Our intention was to determine optimal timing, then do a shot or two with imaging Thomson. We tried shooting Jet B (the only jet that had the potential to work with imaging Thomson) with a 3-ns probe that lasted 30 ns to 33 ns (Shot 70678). Oddly, while Jet C had obtained good EPW data at 30 ns, Jet B did not. Curious to see if timing could solve the problem, we moved the probe to 40 ns to 43 ns (Shot 70679). The IAW signal became clearer, but EPW did not appear. We went later still, to 50 ns to 53 ns (Shot 70680), but the IAW showed signs of reflection, an indication that the density had climbed too high.

Frustrated at our inability to get imaging Thomson data, we switched back to the MIFEDS Configuration. Because we had gotten the best Thomson data at 40 ns, we decided to shoot B individually and B and C colliding, with and without a magnetic field, all at 40 ns, four shots at all (Shots 70681, 70682, 70683, and 70684). We shot

the shots with B field first, because MIFEDS has a tendency to fail and a shot where MIFEDS failed could be used as "no field" shot if we hadn't already done it. This turned out to a wise decision; MIFEDS failed for Shot 70681, but this did not prevent us from getting the four shot matrix we wanted.

B.2.4 Difficulties Encountered

B.2.4.1 Electron Plasma Wave Data

EPW data consistently failed when shooting Jet B alone. When Jets B and C were shot together, good data EPW data obtained. Likewise, when Jet C was shot alone good EPW data was obtained. Since we were able to get good EPW data on several shots throughout day, this clears LLE of any blame for the problem. Clearly, the Thomson scattering set-up was aligned properly. So why did Jet B—and only Jet B—fail to produce EPW data?

One possible explanation is that there was a miscalculation in target design and/or alignment and somehow Jet B was not aimed at TCC. This would explain why experiments with B and C together and the single shot with C alone worked, while the shots with B alone failed. But the IAW data from shots with B alone were successful. In particular, Shots 70681 and 70682 returned very clear data, so there must have been some plasma at TCC to scatter the probe beam.

B.2.4.2 Target Design

As noted above, the MIFEDS Configuration target was built in one pice with the MIFEDS support, something that had not been done before. We were dissatisfied with the alignment precision this decision afforded us. While the MIFEDS system is sufficiently precise to align a current loop in the target chamber, it cannot rotate the target and turned out not to be precise enough to align an experimental target. For subsequent experiments using MIFEDS, we built experimental targets that were

separate from the MIFEDS coils.

However, it seems unlikely that this alignment problem was responsible for the missed EPW data discussed in B.2.4.1. Both configurations, Imaging Thomson and MIFEDS, failed to get EPW data when Jet B was shot alone, and the Imaging Thomson Configuration was mounted in the H2 target positioner, which has excellent precision.

B.2.4.3 Timing

Once we obtained the proton radiography data (several weeks after shot day) we regretted not going later in time. The images seem to show plasma structures beginning to move into the field of view, but did not show the structures that form at TCC when they collide. This problem underscores the need to do simulations of data prior to shot day to aid in shot timings.

Target	
Material	CH
Solid density	$1.18\,\mathrm{g\,cm^{-3}}$
Cone opening angle	160°
Cone diameter	2 mm
Cone thickness	100 μm
Distance to TCC	4 mm
Spacing between cones	45°
Drive Beams	
Drive beam wavelength	351 nm (3ω)
Number beams	4 per cone
Total drive energy	1800 J
Drive beam shape	1 ns, square
Drive beam radius	352 μm (SG4)
Drive irradiance	$5 \times 10^{14}\,\mathrm{W\,cm^{-2}}$
Proton Backlighter Beams	
BL beam wavelength	351 nm (3ω)
Number beams	16
Total drive energy	7200 J
BL beam shape	1 ns, square
BL beam focus	1.81 mm
4ω Thomson beam	
Wavelength	263.25 nm
Energy	50 J
Shape	1 ns or 3 ns, square
Radius	70 μm (best focus)
Angle between probe and collector	116.8°
TIM assignments	
TIM 1	MIFEDS
TIM 2	Empty
TIM 3	Target positioner (BL)
TIM 4	TSS alignment
TIM 5	CR-39 (Wedge Range Filter)
TIM 6	Thomson scattering set-up (TSS)
H2	Target positioner (Thom. exp.)

Table B.5: Experimental parameters for August 15, 2013.

Shot Number	SRF	Cone(s) Driven	Driver Timing	Thomson Timing	Proton Timing	Thomson Length	MIFEDS Charged?
70672	44444	B	−18 ns	0 ns	2 ns	1 ns	Yes
70673	45203	B	−25 ns	0 ns	2 ns	1 ns	No
70674	45204	C	−30 ns	0 ns	2 ns	1 ns	No
70678	45211	B	−30 ns	0 ns	-	3 ns	-
70679	43746	B	−40 ns	0 ns	-	3 ns	-
70680	45210	B	−50 ns	0 ns	-	3 ns	-
70681	45205	B	−40 ns	0 ns	2 ns	1 ns	Yes*
70682	45206	B	−40 ns	0 ns	2 ns	1 ns	Yes
70683	45207	B&C	−40 ns	0 ns	2 ns	1 ns	Yes
70684	44574	B&C	−40 ns	0 ns	2 ns	1 ns	No

Table B.6: Shots on August 15, 2013. *MIFEDS was charged for Shot 70681, but it failed and this was a no-field shot.

Shot Number	SRF	EPW Data?	IAW Data?	PR Data?	MIFEDS?	Notes
70672	44444	✗	✗	✗	Charged	Too early
70673	45203	✗	✗	✓	Not charged	Faint “bubble” on PR
70674	45204	✓	✓	✓	Not charged	Good TS, bubble on PR
70678	45211	✗	✓	-	-	Marginal IAW data
70679	43746	✗	✓	-	-	Very good IAW data
70680	45210	✗	✓	-	-	Marginal IAW data
70681	45205	✗	✓	✓	Failed	Good IAW, crisp bubble
70682	45206	✗	✓	✓	Charged	Good IAW, garbled bubble
70683	45207	✓	✓	✓	Charged	Good TS, two bubbles
70684	44574	✓	✓	✗	Not charged	Good TS, PR failed

Table B.7: Data from August 15, 2013.

B.3 May 2014 Shot Day

B.3.1 Collaboration

The decision to pursue a scaled accretion shock in the laboratory was made with the intention of building a collaboration with Patrick Hartigan, an astrophysicist from Rice University who became a Co-Primary Investigator with Carolyn Kuranz. Mario Manuel also joined our group as a post-doctoral fellow around that time. The scaling work detailed in Chapter II was completed during this time period. Andy Liao, a graduate student from Rice, completed some simulations related to timing using the code EPOCH.

Other than the addition of Rice, little about the collaboration changed from August 2013 (Section B.2.1). Sallee Klein lead target manufacturing; Chikang Li lead proton radiography; Gennady Fiksel lead MIFEDS support; and Dustin Froula and Steve Ross provided insights for Thomson scattering.

B.3.2 Configuration

There were two configurations for the May 2014 shot day: an Imaging Thomson Configuration and an Accretion Configuration, see Table B.8. Both configurations created plasma jets under identical conditions: a thin CH cone was rear irradiated by seven full power OMEGA beams. The Imaging Thomson Configuration, which we shot for the first half of the day, aimed the jet along the 4ω Thomson probe beam in order to study plasma properties. The Accretion Shock Configuration, which we shot for the second half of the day, aimed the jet towards a solid block and imaged the resulting shock with proton radiography. Table B.9 lists the experimental parameters of May 8, 2014.

The Imaging Thomson Configuration consisted single target in the chamber to create a plasma jet, see Figure B.4. The design was based on the successful design of

	Imaging Thom. Config.	Shock Config.
Primary purpose	Imaging Thomson	Scaled Acc. Shock
Launch mechanism	Rear irrad., 7 beams	Rear irrad., 7 beams
Number jets	1	1
Impact surface?	No	Yes
Magnetic field?	Yes, MIFEDS	No
Thomson scattering?	Imaging	No
Proton radiography?	No	Yes
Targets in chamber	1 (exp.)	3 (exp., BL, MIFEDS)

Table B.8: Similarities and differences for the two configurations on May 8, 2014.

April 2012 (see Figure 3.6): a cone was machined into one side of an acrylic block. With such a simple target design, alignment errors such as we experienced in August 2013 were nearly impossible. As seen in Figure B.4, the Thomson probe beam fired along the length of the jet; this set-up is identical to that of Figure A.2.

The Accretion Shock Configuration has been discussed at length in Chapter IV.

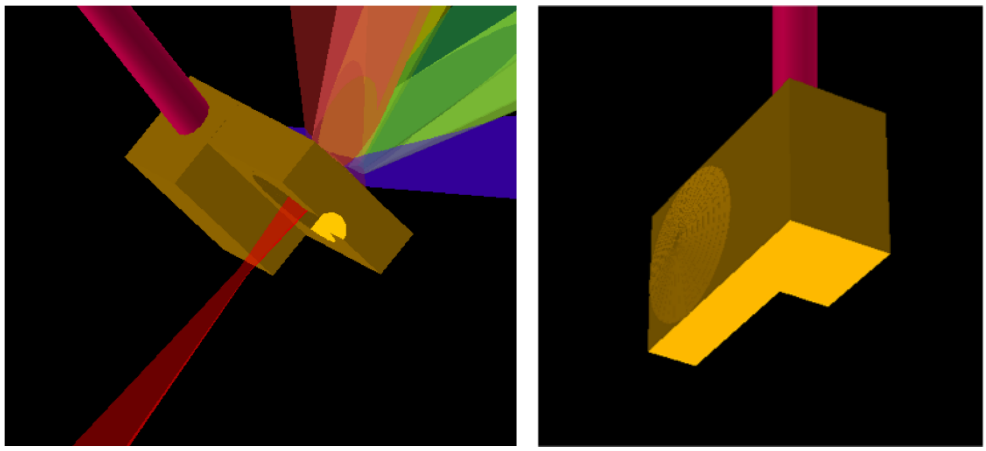

Figure B.4: CAD renderings of the Imaging Thomson Configuration from May 8, 2014. Laser beams are shown in the left view, but omitted from the right view.

B.3.3 Shot Sequence

We began the day with the Imaging Thomson Configuration (OMEGA staff always prefer to have Thomson shots early because of the set-up time needed). We experimented with different timings to find the lower and upper timing limits to get-

ting Thomson scattering data. We found that 16 ns was too early. The following shot found that 20 ns produced good IAW data, but our attempt to jump much later, 28 ns failed. The uneven image that we saw suggested that the density had risen too high and the plasma was reflecting the probe beam. We fell back to 24 ns but there was still evidence of reflection. For our fifth and final Thomson shot we repeated the 20 ns shot and again obtained good IAW data.

Frustratingly, we were never able to get EPW data. Our experience was somewhat like that of August 2013, except that shot day used streaked Thomson scattering as well, whereas this shot used imaging Thomson exclusively. This failure is discussed in more detail in the next section.

The second half of the day was dedicated to the Accretion Shock Configuration. We began with a control shot; no field was imposed. We then decided to complete a three by two matrix of shots: 30, 50, and 70 ns, with either a high field (7 T) or a low field (3 T). We did completed the 30-ns and 50-ns shots first. We were told that MIFEDS failed for Shot 73336 (which was intended to be high field, 30 ns), so that shot was repeated, but the proton radiography suggests that there was a field. Having completed the 30-ns and 50-ns portion of the matrix, we moved on to the 70-ns shots, but unfortunately MIFEDS failed for the high field 70-ns shot.

Table B.10 lists the parameters for the thirteen shots on May 8, 2014 and Table B.11 lists whether data was successful.

Target	
Material	CH
Solid density	$1.18\,\mathrm{g\,cm^{-3}}$
Cone opening angle	160°
Cone diameter	2 mm
Cone thickness	100 μm
Distance to TCC	3 mm
Drive Beams	
Drive beam wavelength	351 nm (3ω)
Number beams	7
Total drive energy	3150 J
Drive beam shape	1 ns, square
Drive beam radius	352 μm (SG4)
Drive irradiance	$8 \times 10^{14}\,\mathrm{W\,cm^{-2}}$
Backlighter Beams	
Drive beam wavelength	351 nm (3ω)
Number beams	15
Total drive energy	6750 J
Drive beam shape	1 ns, square
Drive beam focus	1.81 mm
4ω Imaging Thomson beam	
Wavelength	263.25 nm
Energy	50 J
Shape	0.5 ns, square
Radius	70 μm (best focus)
Angle between probe and collector	116.8°
TIM assignments	
TIM 1	MIFEDS
TIM 2	CR-39
TIM 3	Target positioner (Shock Exp)
TIM 4	TSS alignment/Target positioner (BL)
TIM 5	Particle temporal diagnostic
TIM 6	Thomson scattering set-up (TSS)
H2	Target positioner (Thomson Exp)

Table B.9: Experimental parameters for May 8, 2014. The first half of the day was the Thomson experiment; the second half was the accretion shock experiment.

Shot Number	SRF	Primary Diagnostics	Timing	Notes
73327	47377	4ω TSS	16 ns	Jet barely in range
73328	48648	4ω TSS	20 ns	Good timing
73330	48649	4ω TSS	28 ns	Probe reflected
73331	48650	4ω TSS	24 ns	Probe reflected
73334	48651	4ω TSS	20 ns	Best data
73335	47405	Prot. radio.	30 ns	No MIFEDS
73336	47376	Prot. radio.	30 ns	MIFEDS failed
73337	48652	Prot. radio.	30 ns	MIFEDS, 3 turns, 7 T
73338	48653	Prot. radio.	50 ns	MIFEDS, 3 turns, 7 T
73339	48654	Prot. radio.	30 ns	MIFEDS, 1 turn, 3 T
73340	48655	Prot. radio.	50 ns	MIFEDS, 1 turn, 2.4 T
73341	48656	Prot. radio.	70 ns	MIFEDS, 1 turn, 3 T
73344	48825	Prot. radio.	70 ns	MIFEDS, field failed

Table B.10: Shots on May 8, 2014. Halfway through the day, the configuration changed from imaging Thomson scattering to accretion shock with magnetic field.

Shot Number	SRF	EPW Data?	IAW Data?	TPDI Data?	PR Data	Notes
73327	47377	✗	✓	✗	-	Barely in range
73328	48648	✗	✓	✗	-	In range
73330	48649	✗	✗	✗	-	Too dense
73331	48650	✗	✗	✗	-	Too dense
73334	48651	✗	✓	✗	-	In range
73335	47405	-	-	-	✓	Control; no field
73336	47376	-	-	-	✗	Protons off CR-39
73337	48652	-	-	-	✗	Protons off CR-39
73338	48653	-	-	-	✗	Protons off CR-39
73339	48654	-	-	-	✗	Protons off CR-39
73340	48655	-	-	-	✗	Protons off CR-39
73341	48656	-	-	-	✗	Protons off CR-39
73344	48825	-	-	-	✓	Field failed

Table B.11: Data on May 8, 2014.

B.3.4 Difficulties Encountered

B.3.4.1 EPW Data Failure

Our experience with EPW data was similar to that of August 2013: when the jet was aligned along the 4ω probe beam, IAW data was obtained but not EPW. In August 2013, both streaked and imaging Thomson scattering were attempted in the probe-parallel-to-jet configuration; both failed. In May 2014 only imaging Thomson scattering was attempted in the probe-parallel-to-jet configuration, and once again it failed. In August 2013, because we had three potential jets, we had the option of falling back to a slightly different configuration with the jet coming on from the side. That configuration worked, although it only worked for streaked Thomson, obviously.

Figure B.5 compares failed EPW data from August 2013 and May 2014. The August 2013 data shows the time fiducial (the dots along the top and bottom of the image) because this is streaked data, and no discernible scattered spectrum. The May 2014 data shows no time fiducial—this is imaging data—but there is a mysterious extended shape in the middle of the image that looks nothing like a scattered EPW spectrum.

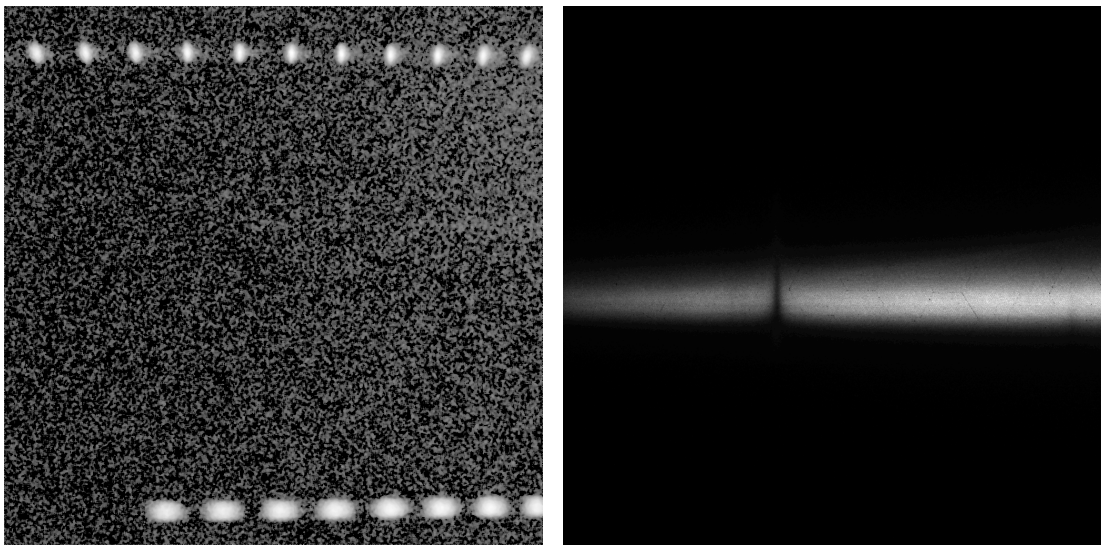

Figure B.5: EPW data from August 2013 and May 2014. Left: EPW data from Shot 70678, August 2013. Right: EPW data from Shot 73334, May 2014.

B.3.4.2 Proton Deflection

The images obtained from May 2014 are, with the exception of the control shots for which there was no magnetic field, extremely odd and riddled with strange shapes that look nothing like the data we were expecting, see Figure 5.7. This turned out to be due to protons being deflected off the CR-39; see Section 5.4.

B.4 May and October 2015 Shot Days

B.4.1 Collaboration

Because May 2015 was a repeat of May 2014 with the proton radiography deflection problem fixed, the collaboration was basically unchanged from May 2014, see Section B.3.1. Michigan graduate student Joseph Levesque joined the CLEAR magnetized plasmas projects and MIT graduate student Hong Sio joined to assist with proton radiography.

B.4.2 Configuration

The configuration in May 2015 was nearly identical to that of May 2014, see Chapter IV. Table B.12 lists the experimental parameters; some TIM assignments were changed compared to May 2014.

Target	
Material	CH
Solid density	$1.18\,\mathrm{g\,cm^{-3}}$
Cone opening angle	160°
Cone diameter	2 mm
Cone thickness	$100\,\mu$m
Drive Beams	
Drive beam wavelength	351 nm (3ω)
Number beams	7 or 1
Total drive energy	3150 J or 450 J
Drive beam shape	1 ns, square
Drive beam radius	$352\,\mu$m (SG4)
Proton Backlighter Beams	
BL beam wavelength	351 nm (3ω)
Number beams	18
Total drive energy	8100 J
BL beam shape	1 ns, square
BL beam focus	0 mm, best focus (see note)
TIM assignments	
TIM 1	MIFEDS
TIM 2	Target positioner (BL.)
TIM 3	Target positioner (Exp.)
TIM 4	CR-39 (Wedge range filter)
TIM 5	Target positioner (Shield)
TIM 6	Thomson scattering (TPDI only)
H2	Not used

Table B.12: Experimental parameters for May 14, 2015. The October 27, 2015 shots were the same, except the experiment was moved to the H2 target positioner and MIFEDS and proton backlighting were dropped. Note: using best focus for the proton backlighter was a mistake that was not caught until well after shot day, see Section B.4.4.3.

B.4.3 Shot Sequence

On previous shot days, we had used seven full power drive beams to launch the plasma jets. We initially used seven beams on this shot day as well, see Shots 77250 and 77251, see Table B.13. Shot 77254 was a control shot of proton radiography without a jet. During that shot cycle, we reassessed our results from the first two shots and decided to fall back to using one full power drive beam in order to reduce the velocity of the incoming and thereby bring down the plasma β. After using one shot to get timing right, we settled on doing six shots at 20 ns, 40 ns, and 60 ns, with and without magnetic fields.

Table B.14 contains a list of successful data taken. While TPDI data was generally good, we consistently had problems with proton generation, see Section B.4.4.3. We found that most of the proton images obtained are identical to the control shot. The one exception is Shot 77254, the only seven-beam shot to use proton radiography.

Shot Number	SRF	Field Imposed	Drive Beams	Driver Timing	Proton Timing	TPDI Timing
77250	51957	0 T	7	−20 ns	-	+3 ns
77251	53198	0 T	7	−10 ns	-	+3 ns
77254	51955	8 T	-	-	0 ns	+3 ns
77255	51544	8 T	7	−10 ns	0 ns	+3 ns
77256	53202	8 T	1	−20 ns	0 ns	+3 ns
77258	53203	8 T	1	−40 ns	0 ns	+3 ns
77259	53205	8 T	1	−60 ns	0 ns	+3 ns
77260	51954	0 T	1	−20 ns	0 ns	+3 ns
77261	53199	0 T	1	−47 ns	0 ns	−4 ns
77262	53200	0 T	1	−60 ns	0 ns	+3 ns
79221	54550	0 T	1	−43 ns	-	0 ns
79222	55517	0 T	1	−43 ns	-	0 ns

Table B.13: Shots on May 2015 and October 2015. Shots on May 14, 2015 (Shots 77250 through 77262) and October 27, 2015 (Shots 79221 and 79222).

Shot Number	SRF	TPDI Filtering	TPDI Data?	PR Data?	Notes
77250	51957	ND 2.0 (see note)	✓	-	Damaged camera
77251	53198	ND 3.0+LP385	✗	-	Too early
77254	51955	ND 3.0+LP385	✓	✓	Control shot
77255	51544	ND 3.0+LP385+VG380	✓	✓	Only good PR image
77256	53202	ND 3.0+LP385+VG380	✓	✗	No protons
77258	53203	ND 3.0+LP385+VG380	✓	✗	No protons
77259	53205	ND 3.0+LP385+VG380	✓	✗	No protons
77260	51954	ND 3.0+LP385+VG380	✓	✗	Clear TPDI
77261	53199	ND 3.0+LP385+VG380	✗	✗	TPDI failed
77262	53200	ND 3.0+LP385+VG380	✓	✗	Clear TPDI
79221	54550	ND 2.0+LP385	✗	-	Overfiltered
79222	55517	LP385	✓	-	Overfiltered

Table B.14: Data from May 2015 and October 2015. Data on May 14, 2015 (Shots 77250 through 77262) and October 27, 2015 (Shots 79221 and 79222). Note: the CCD sustained damage during Shot 77250 due to under-filtering.

B.4.4 Difficulties Encountered

B.4.4.1 Target Positioning

We encountered a problem with target positioning. While the source of this problem was LLE, not our experimental design, it underscored the need to do test alignments on OMEGA. During the test alignment the day before shot day, LLE discovered an interference between the MIFEDS support arm and the shield stalk. This interference was not present in the aligned configuration, but it made alignment impossible. (There was no way for our research group to anticipate this as LLE designs their own alignment procedures.) Fortunately, we were able to move the shield to a different target positioner and shots the next day were unaffected.

B.4.4.2 Visible Light Imaging

There is evidence that the MIFEDS coils obscured the view of the experiments. The experiment was designed such that the entire experimental volume was visible from TIM 6 (TPDI). However, the fiducial notch is readily observed in the no-field shots (where MIFEDS was not inserted into the chamber) and appears obscured in the shots with MIFEDS, see Figure B.6. This is either due to the coils squeezing together as MIFEDS is fired or to glow from the coils themselves drowning out the light coming from the experimental target.

B.4.4.3 Proton Radiography

We consistently got low neutron counts from the Nuclear Diagnostic Inserter (NDI), about 8×10^7 neutrons compared to 5×10^8 neutrons in May 2014. We were unable to track down the root of the problem on shot day. During the October 2015 day (which was largely devoted to another campaign), we discovered during conversations with OMEGA that we had had the backlighter beams focused incor-

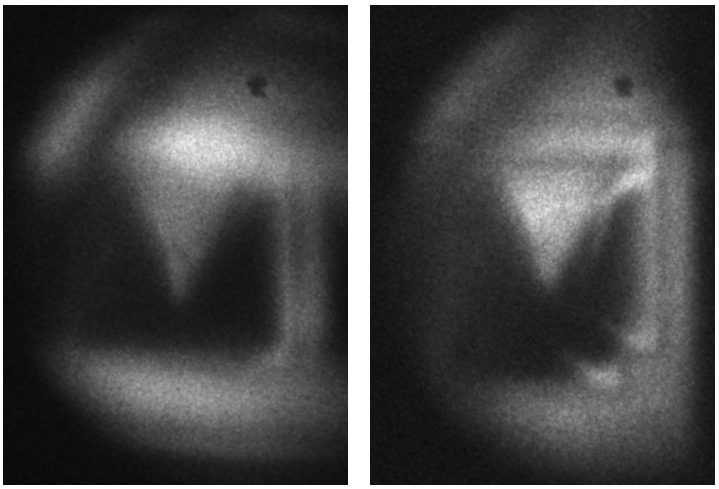

Figure B.6: Visible light images from May 2015 with and without the fiducial visible. Left: The fiducial notch is not visible in Shot 77256, which used MIFEDS. Right: The fiducial notch is visible in the lower right-hand corner of Shot 77260, a no-field shot where MIFEDS was not inserted into the chamber.

rectly. We had selected a focus of 0.00 mm (that is, best focus) while we should have set the focus to 1.81 mm. That would de-focus the backlighter beams such that they evenly irradiate the backlighter capsule. At best focus, they crack the capsule before it implodes, fusion is disrupted, and the proton count drops.

APPENDIX C

Data from April 2012

C.1 65762

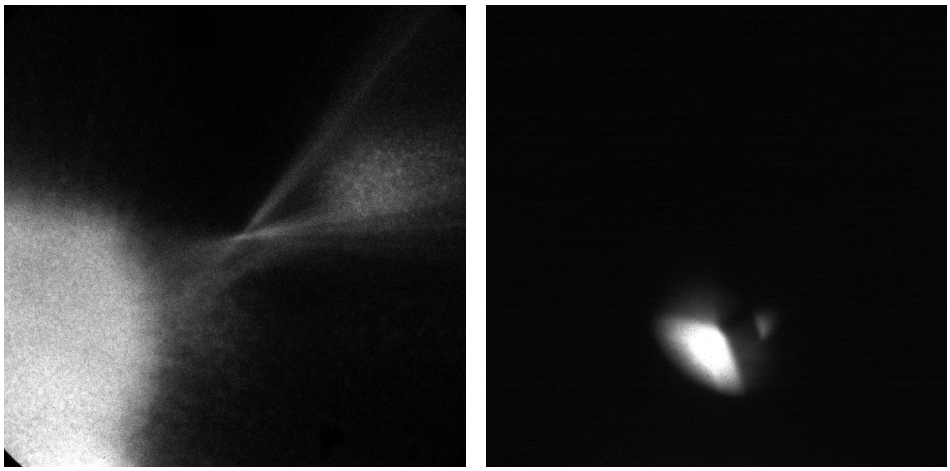

Figure C.1: GOI and TPDI of 65762. GOI (left), 7 ns after drive, and TPDI (right), 17 ns after drive, images from 65762. A single jet shot moving away from the viewer in TIM 6. Compare this TPDI to that of 65763. Here the laser spot is brighter and the jet, which is peeking out from behind the target, is barely visible.

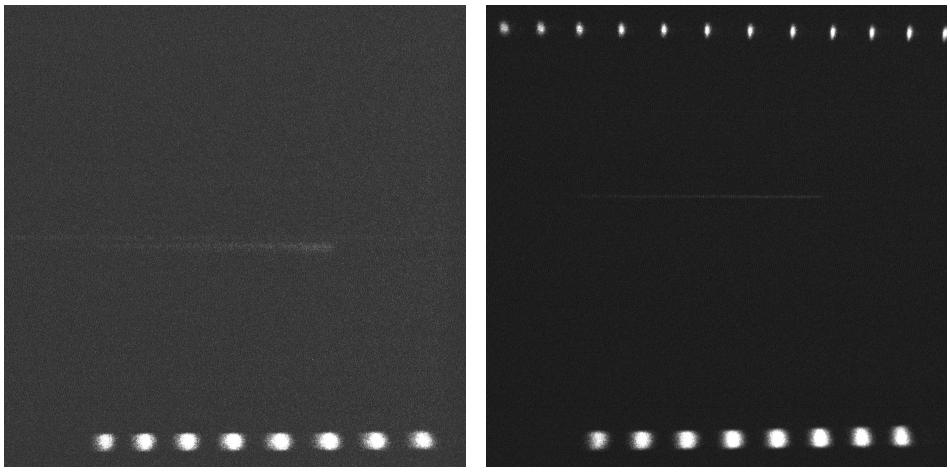

Figure C.2: Thomson spectra of 65762. EPW (left) and IAW (right) images from 65762. Probe beam fired from 7 to 10 ns after drive. No usable spectra from this shot; the probe beam was fired too early. The jet had yet to reach TCC.

C.2 65763

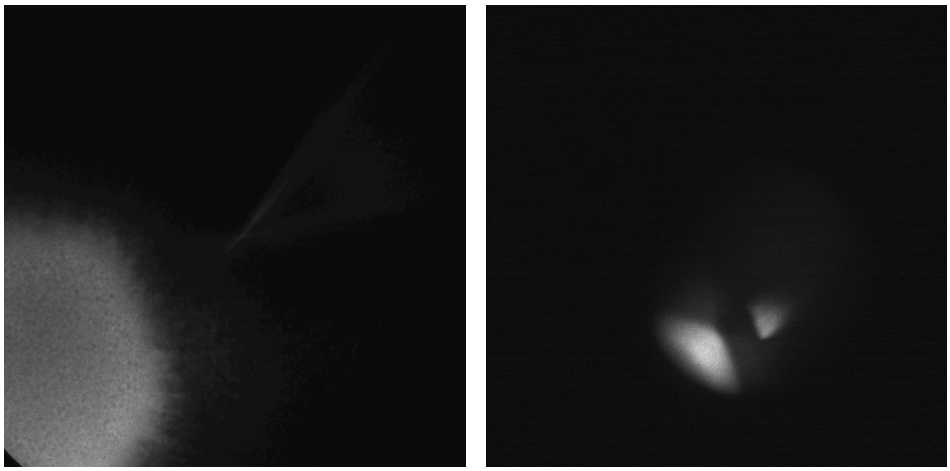

Figure C.3: GOI and TPDI of 65763. GOI (left), 9 ns after drive, and TPDI (right), 22 ns after drive, images from 65763. A single jet shot moving away from the viewer in TIM 6. Compare this TPDI to that of 65762. Because this shot was 5 ns later, the laser spot is dimmer and the jet has moved farther out from behind the target.

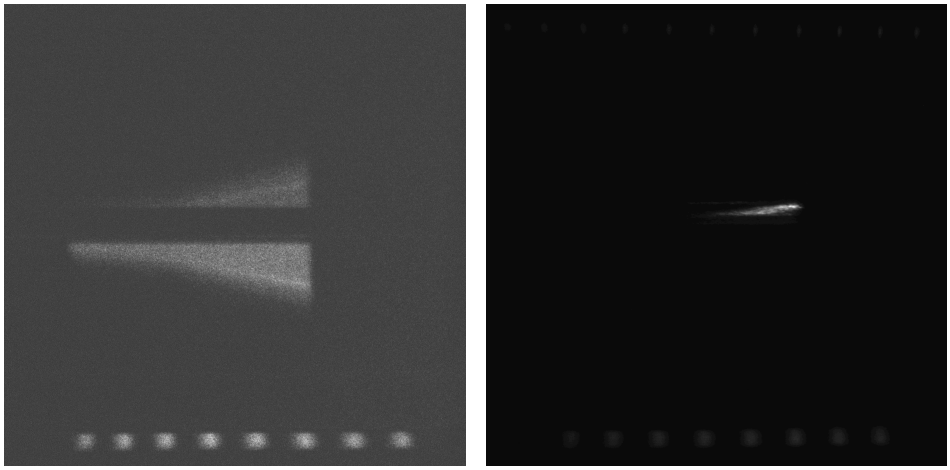

Figure C.4: Thomson spectra of 65763. EPW (left) and IAW (right) images from 65763. Probe beam fired from 12 to 15 ns after drive. Note that the IAW fits show a negative velocity; this is because the jet is moving away from the spectrograph in TIM 6.

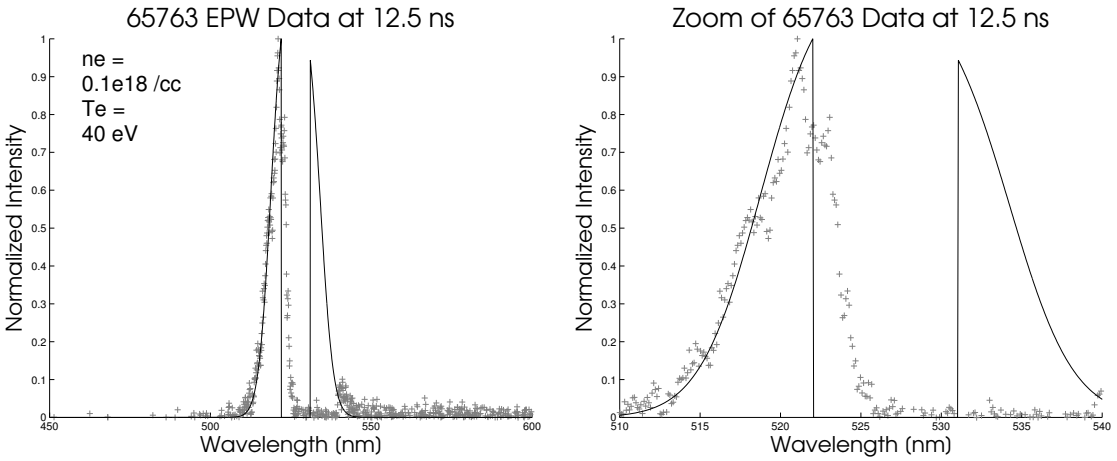

Figure C.5: 65763 EPW data at 12.5 ns

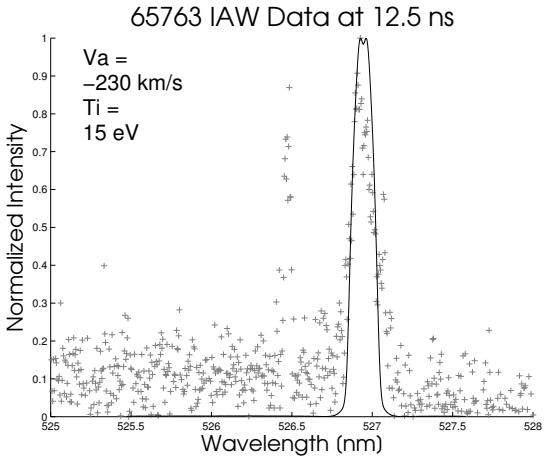

Figure C.6: 65763 IAW data at 12.5 ns

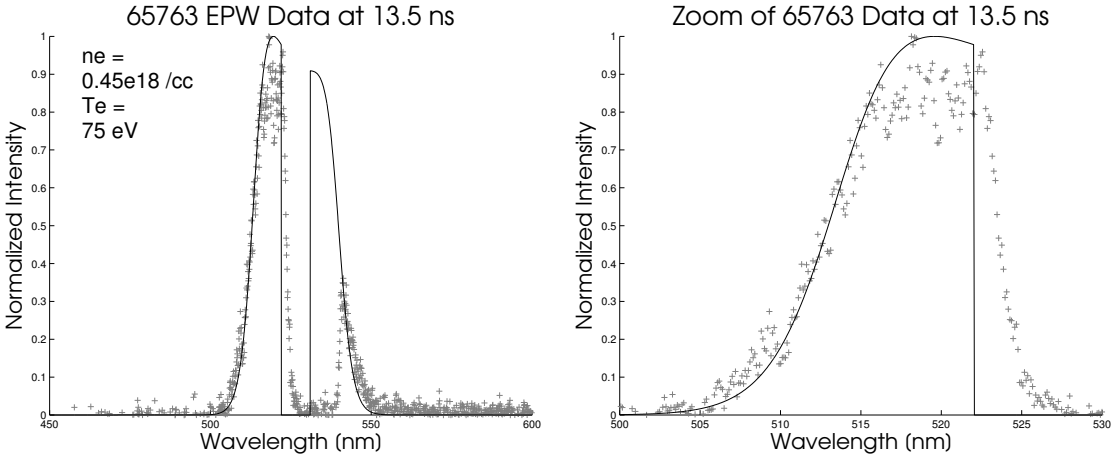

Figure C.7: 65763 EPW data at 13.5 ns

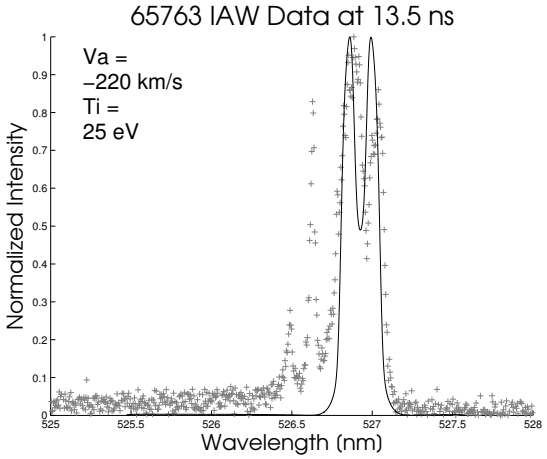

Figure C.8: 65763 IAW data at 13.5 ns

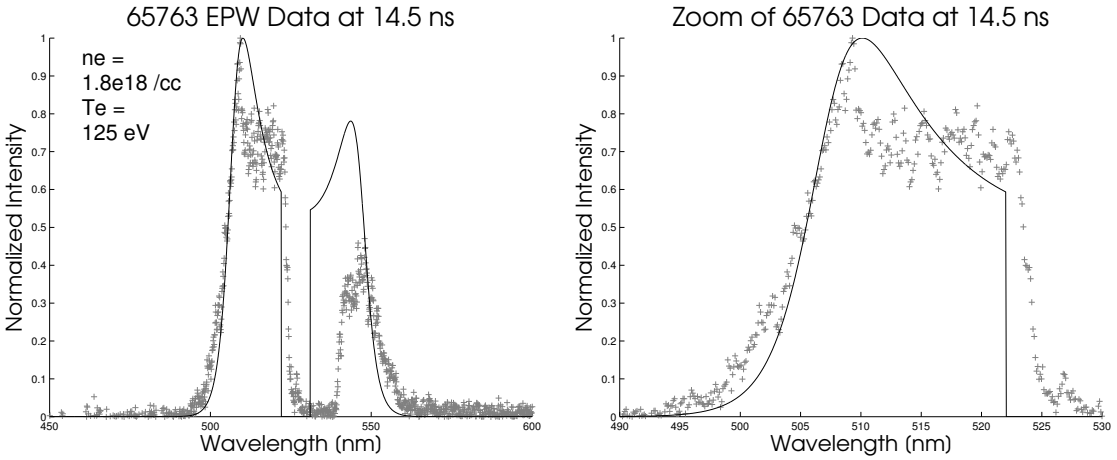

Figure C.9: 65763 EPW data at 14.5 ns

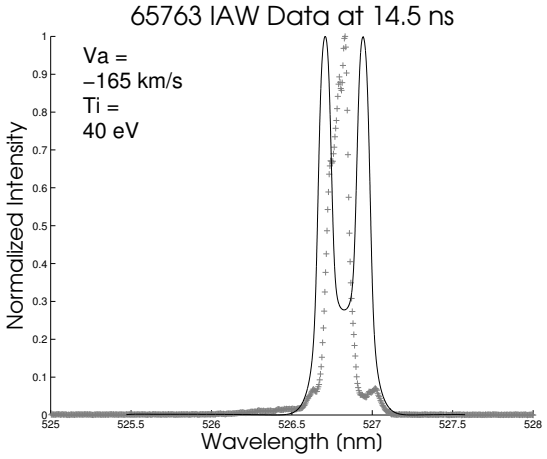

Figure C.10: 65763 IAW data at 14.5 ns

C.3 65764

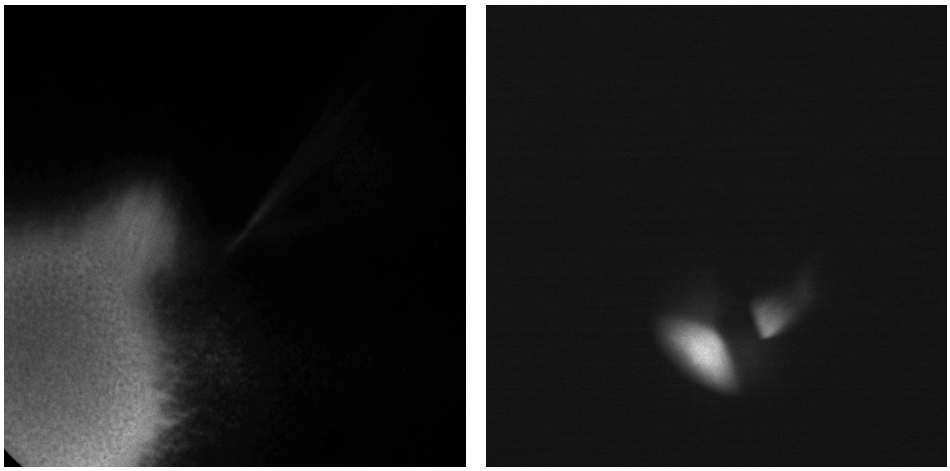

Figure C.11: GOI and TPDI of 65764. GOI (left), 12 ns after drive, and TPDI (right), 25 ns after drive, images from 65764. Single jet moving away from the viewer in TIM 6. This TPDI is very similar to 65763, as it is only 3 ns later.

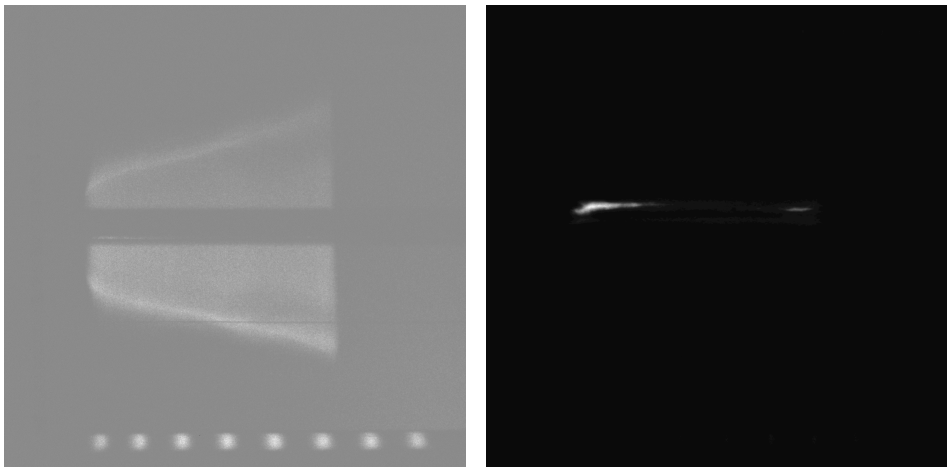

Figure C.12: Thomson spectra for 65764. EPW (left) and IAW (right) images from 65764. Probe beam fired from 15 to 18 ns. Note that no IAW data was obtained at the earliest time, 15.5 ns.

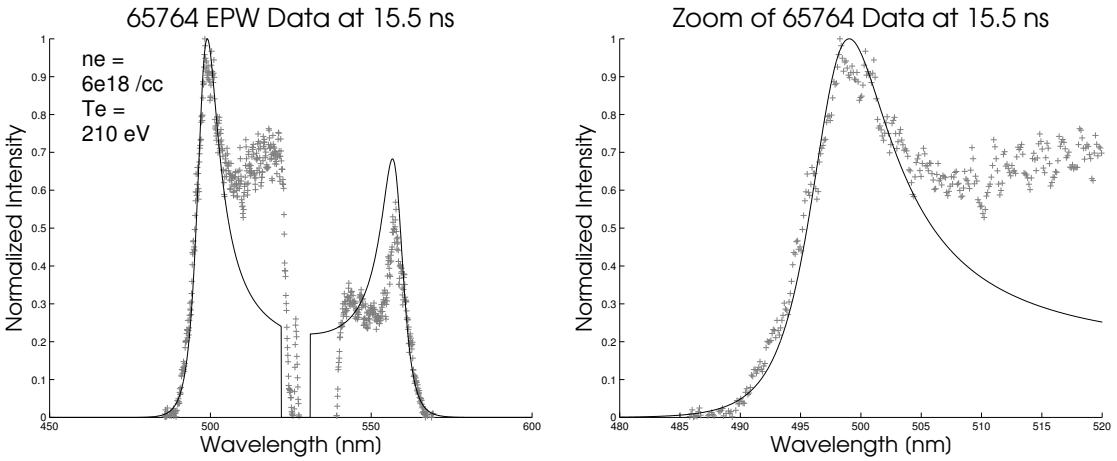

Figure C.13: 65764 EPW data at 15.5 ns

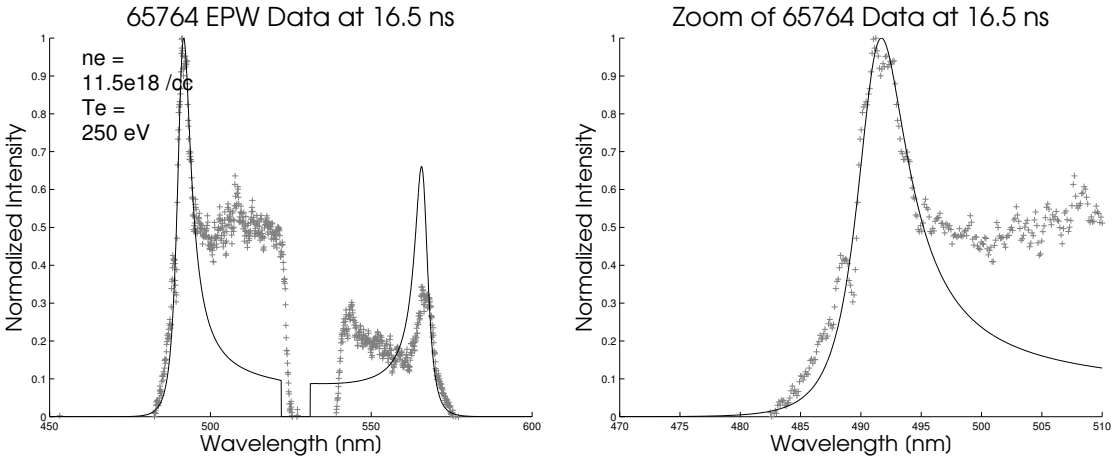

Figure C.14: 65764 EPW data at 16.5 ns

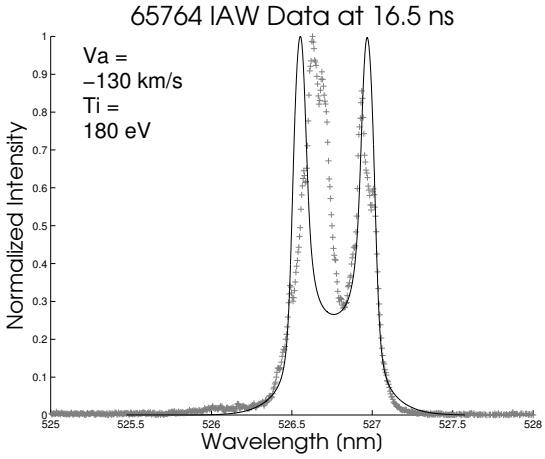

Figure C.15: 65764 IAW data at 16.5 ns

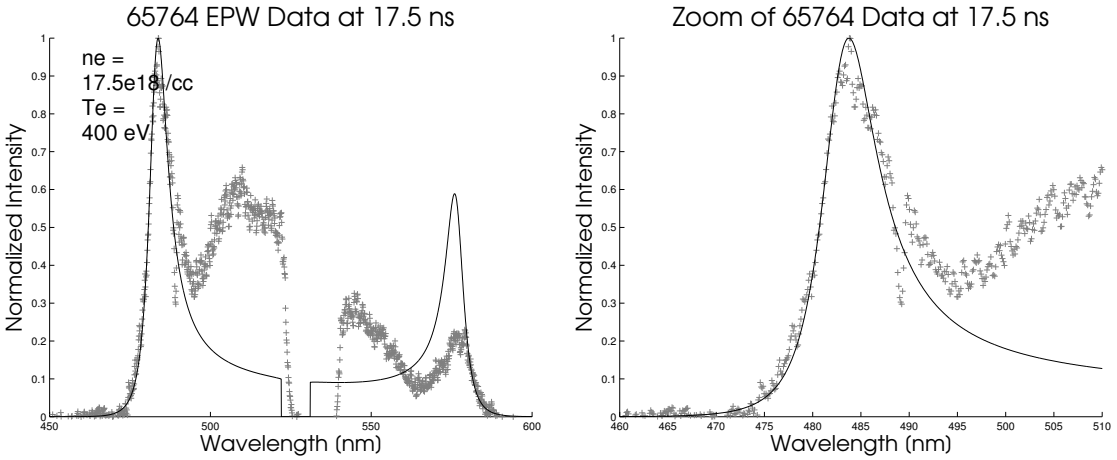

Figure C.16: 65764 EPW data at 17.5 ns

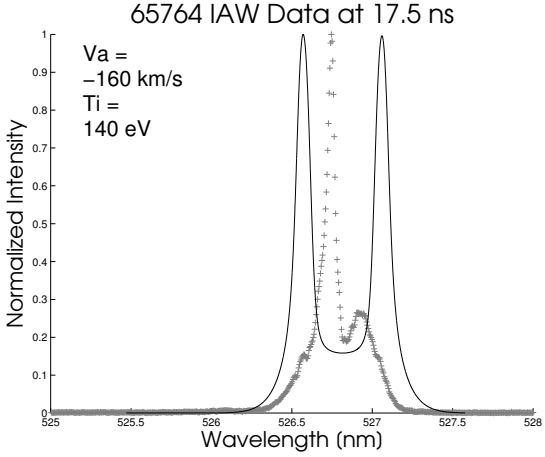

Figure C.17: 65764 IAW data at 17.5 ns

C.4 65765

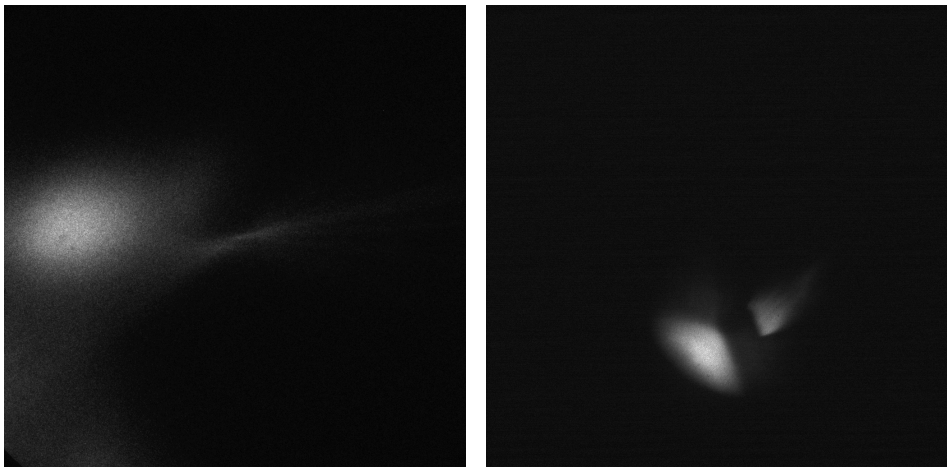

Figure C.18: OI and TPDI of 65765. GOI (left), 20 ns after drive, and TPDI (right), 25 ns after drive, images from 65765. Single jet moving away from the viewer in TIM 6. The TPDI ought to be identical to 65764.

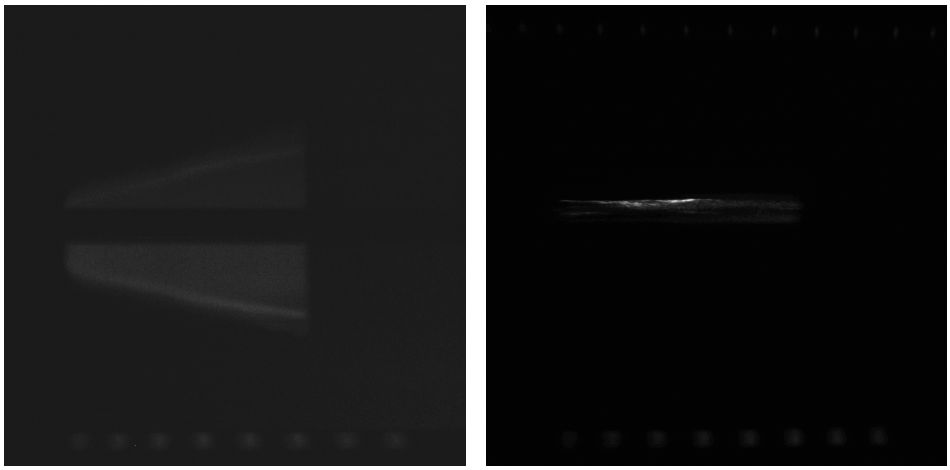

Figure C.19: Thomson spectra for 65765. EPW (left) and IAW (right) images from 65765. Probe beam fired from 15 to 18 ns. Note that there is no IAW data at 15.5 ns.

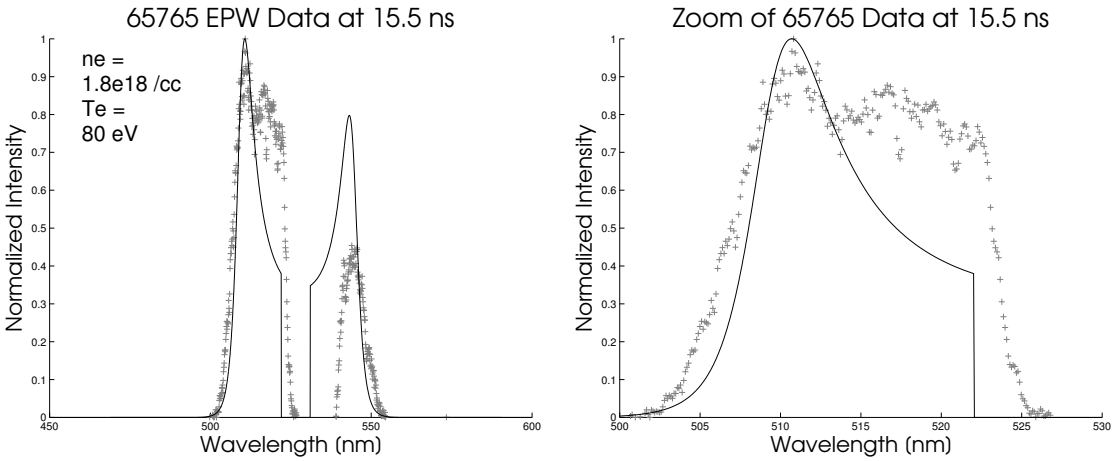

Figure C.20: 65765 IAW data at 15.5 ns

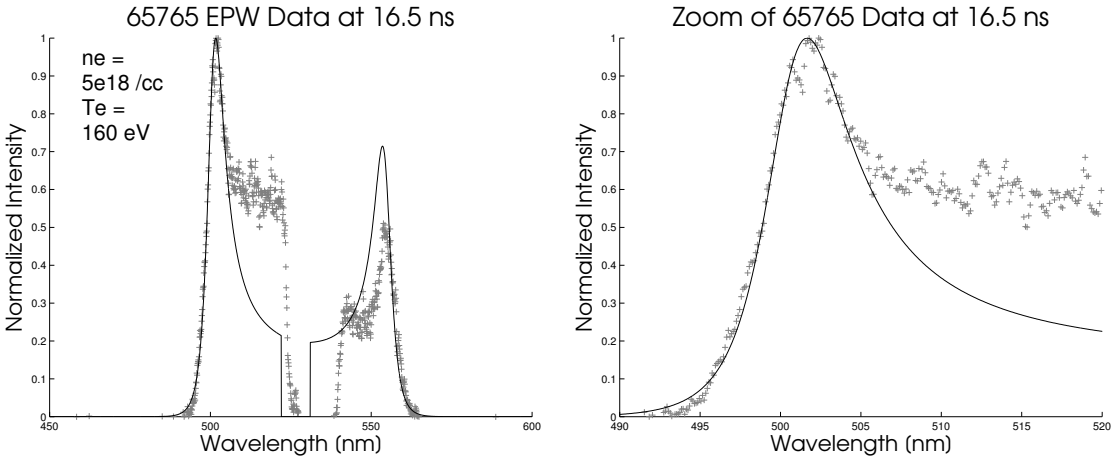

Figure C.21: 65765 EPW data at 16.5 ns

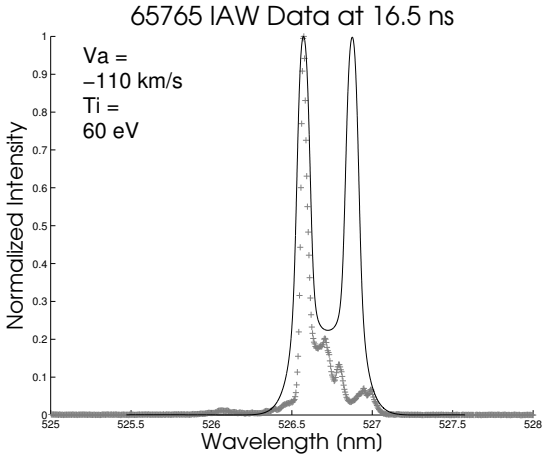

Figure C.22: 65765 IAW data at 16.5 ns

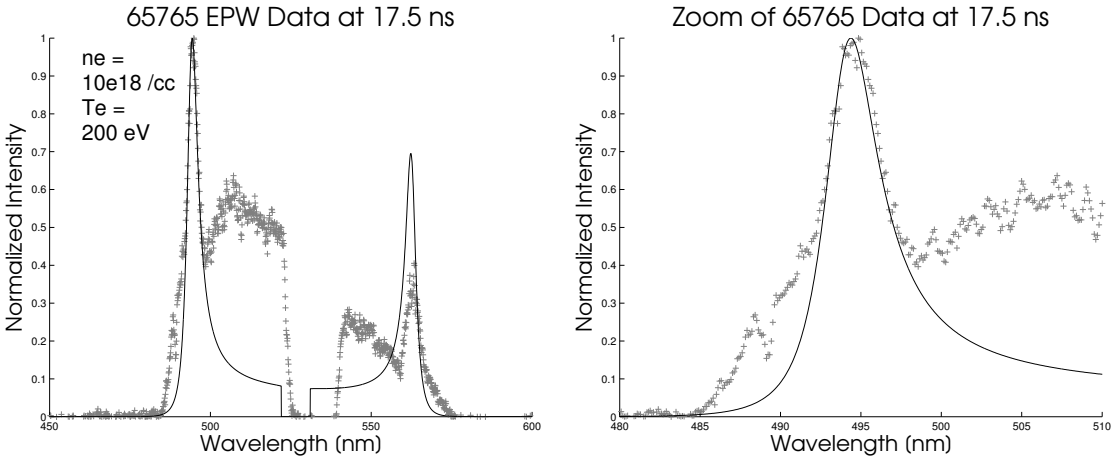

Figure C.23: 65765 EPW data at 17.5 ns

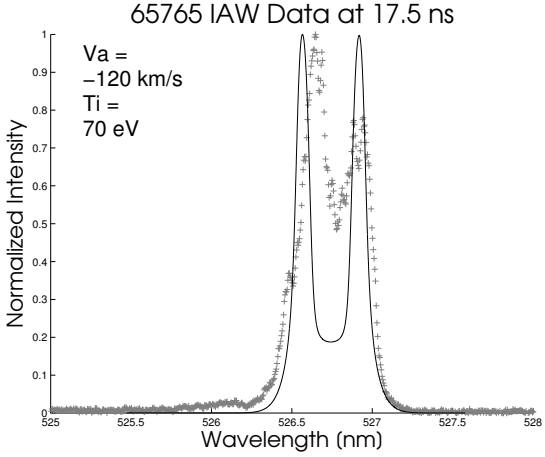

Figure C.24: 65765 IAW data at 17.5 ns